Inorganic Chemistry

Article

pubs.acs.org/IC

What Controls the Magnetic Exchange and Anisotropy in a Family of Tetranuclear $\{Mn^{II}_2Mn^{III}_2\}$ Single-Molecule Magnets?

Kuduva R. Vignesh,[†] Stuart K. Langley,[‡] Christopher J. Gartshore,[§] Boujemaa Moubaraki,[§] Keith S. Murray,*[,§] and Gopalan Rajaraman*[,∥]

[†]IITB-Monash Research Academy, IIT Bombay, Mumbai 400076, India

[§]School of Chemistry, Monash University, Clayton, Victoria 3800, Australia

[‡]School of Science and the Environment, Chemistry Division, Manchester Metropolitan University, Manchester, United Kingdom

[∥]Department of Chemistry, Indian Institute of Technology Bombay, Mumbai 400076, India

Supporting Information

ABSTRACT: Twelve heterovalent, tetranuclear manganese(II/III) planar diamond or "butterfly" complexes, **1**−**12**, have been synthesized and structurally characterized, and their magnetic properties have been probed using experimental and theoretical techniques. The 12 structures are divided into two distinct "classes". Compounds **1**−**8** place the Mn(III), $S = 2$, ions in the body positions of the butterfly metallic core, while the Mn(II), $S = 5/2$, ions occupy the outer wing sites and are described as "Class 1". Compounds **9**−**12** display the reverse arrangement of ions and are described as "Class 2". Direct current susceptibility measurements for **1**−**12** reveal ground spin states ranging from $S = 1$ to $S = 9$, with each complex displaying unique magnetic exchange parameters (J). Alternating current susceptibility measurements found that that slow magnetic relaxation is observed for all complexes, except for **10** and **12**, and display differing anisotropy barriers to magnetization reversal. First, we determined the magnitude of the magnetic exchange parameters for all complexes. Three exchange coupling constants (J_{bb}, J_{wb}, and J_{ww}) were determined by DFT methods which are found to be in good agreement with the experimental fits. It was found that the orientation of the Jahn−Teller axes and the Mn−Mn distances play a pivotal role in determining the sign and strength of the J_{bb} parameter. Extensive magneto-structural correlations have been developed for the two classes of $\{Mn^{II}_2Mn^{III}_2\}$ butterfly complexes by varying the Mn_b−O distance, Mn_w−O distance, Mn_b−O−Mn_b angle (α), Mn_b−O−Mn_b−O dihedral angle (γ), and out-of-plane shift of the Mn_w atoms (β). For the magnetic anisotropy the DFT calculations yielded larger negative D value for complexes **2**, **3**, **4**, and **6** compared to the other complexes. This is found to be correlated to the electron-donating/withdrawing substituents attached to the ligand moiety and suggests a possible way to fine tune the magnetic anisotropy in polynuclear Mn ion complexes.

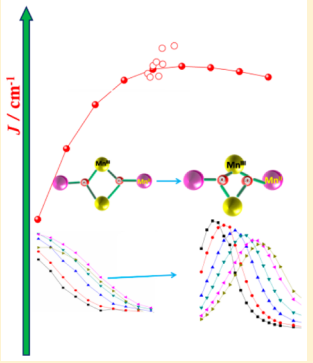

INTRODUCTION

The structural and magnetic investigations of discrete mixed-valence manganese "butterfly" complexes possessing a $\{Mn^{II}_2Mn^{III}_2\}$ magnetic core continue to attract interest due to the fact that these compounds were some of the first single-molecule magnets (SMMs) studied.[1] These butterfly complexes, however, are not limited to the above Mn(II)/Mn(III) ion type, with homovalence $\{Mn^{III}_4\}$ and mixed-valence $\{Mn^{III}_3Mn^{IV}\}$ magnetic cores also having been reported.[2] Molecules that display SMM behavior reveal slow relaxation of the magnetization vector and magnetic hysteresis as a result of an energy barrier to spin inversion.[3] In manganese-based complexes this is due to a large spin ground state (S) combined with an axial magnetic anisotropy given by a negative zero-field splitting parameter (D). The energy barrier displays the relationship $U = S^2|D|$ and at low enough temperatures allows for the manipulation of the spin orientation by the magnetic field, resulting in several important potential applications.[4] Mixed-valent $\{Mn^{II}_2Mn^{III}_2\}$ butterfly complexes often reveal the necessary requirements to observe SMM behavior, with the maximum possible ground spin state of $S = 9$ being a common observation for this system.[1j] These complexes also display a large enough anisotropy to block the magnetization vector along an easy axis with D values generally ranging from −0.15 to −0.6 cm^{-1}.[5] The key attraction that makes these polynuclear complexes of particular interest to study is that it is possible, due to the relatively small nuclearity of these cluster types, to perform in-depth analyses of the magnetic interactions and of the SMM parameters. These are, therefore, excellent model complexes for determination of the factors which can affect the SMM behavior and, ultimately, allow one to tune the parameters favorably. These butterfly complexes gain their name from the arrangement of their tetranuclear core, which contains four metal ions. Two are placed in the central "body", and two in the outer "wing" positions, with two oxygen ligands of μ_3-η^1:η^1:η^1 connectivity bridging to all four ions (see Figure 1).[1a,b,j,2,6] The μ_3-O atoms are typically O^{2-}or OH^- but can

Received: October 18, 2016
Published: February 3, 2017

DOI: 10.1021/acs.inorgchem.6b02527
Inorg. Chem. 2017, 56, 1932−1949

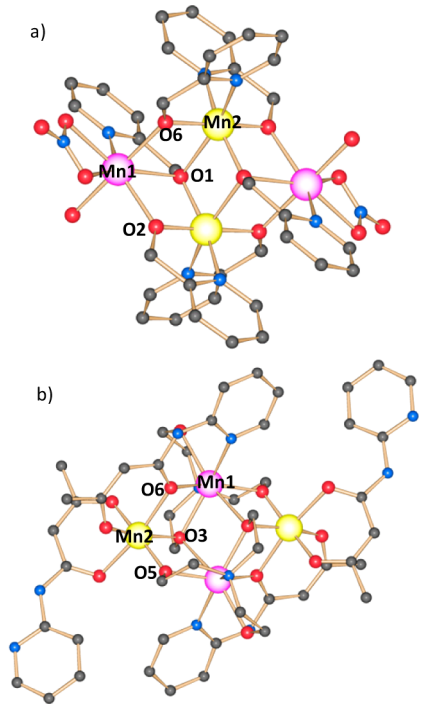

Figure 1. Molecular structure of compounds (a) **1** (Class 1) and (b) **9** (Class 2). H atoms and solvent molecules are omitted for clarity. Color scheme; Mn^{III}, yellow; Mn^{II}, pink; O, red; N, blue; C, gray.

also be derived from alkoxide O atoms.[6b] It has also been shown that sulfide bridges can be used.[6e] These complexes can be homometallic[1b,2d] or heterometallic with differing metal atoms located on the wings and body positions of the complex.[6e] Due to the interest in SMMs and manganese polynuclear complexes in particular coupled with a near total lack of underlying theory, we have undertaken a combined experimental and density functional theoretical (DFT) approach focusing on 12 analogous mixed-valence manganese(II/III) butterfly complexes of formulas $[Mn^{II}_2Mn^{III}_2(hmp)_6(NO_3)_2(H_2O)_2](O_3SC_6H_4CH_3)_2$ (**1**), $[Mn^{II}_2Mn^{III}_2(hmp)_6(NO_3)_2(O_3SC_6H_4CH_3)_2]$ (**2**), $[Mn^{II}_2Mn^{III}_2(teaH)_2(teaH_2)_2(iso)_2](NO_3)_2$ (**3**), $[Mn^{II}_2Mn^{III}_2(teaH)_2(teaH_2)_2(pdca)_2]$ (**4**), $[Mn^{II}_2Mn^{III}_2(teaH)_2(teaH_2)_2(piv)_2](iso)_2$ (**5**), $[Mn^{II}_2Mn^{III}_2(tea\text{-}4\text{-}nsa)_2(4\text{-}nsa)_2(H_2O)_2]$ (**6**), $[Mn^{II}_2Mn^{III}_2(tea\text{-}o\text{-}van)_2(o\text{-}van)_2(MeOH)_2]$ (**7**), $[Mn^{II}_2Mn^{III}_2(tea\text{-}o\text{-}van)_2(teaH_3)_2](NO_3)_2$ (**8**), $[Mn^{II}_2Mn^{III}_2(teaH)_2(paa)_4](NO_3)_2$ (**9**), $[Mn^{II}_2Mn^{III}_2(teaH)_2(O_2CPh)_4(acac)_2]$ (**10**), $[Mn^{II}_2Mn^{III}_2Co^{III}_2(teaH)_4(OMe)_2(acac)_4](NO_3)_2$ (**11**), and $[Mn^{II}_2Mn^{III}_2(teaH)_2(MeOH)_4(acac)_4](ClO_4)_2$ (**12**) (where hmpH = 2-hydroxymethylpyridine, $teaH_3$ = triethanolamine, isoH = isonicotinic acid, $pdcaH_2$ = 3,4-pyridinedicarboxylic acid, pivH = pivalic acid, tea-4 $nsaH_4$ = 2-({2-[bis(2-hydroxyethyl)amino]ethoxy}hydroxymethyl)-4-nitrophenol, 4-nsaH = 4-nitrosalicylaldehyde, tea-o-$vanH_4$ = 2-({2-[bis(2-hydroxyethyl)amino]ethoxy}hydroxymethyl)-6-methoxyphenol, o-vanH = *o*-vanillin, paaH = 2-pyridylacetylacetamide, acacH = acetylacetone). We used these complexes, reported herein, to determine what structural features affect the key SMM parameters, *S* and *D*. Nine of these complexes are newly synthesized (**1**−**8** and **10**), while three have been reported previously (**9**, **11**, and **12**).[1h−j] Due to the differences in Mn ion arrangement for **1**−**12** the compounds have been divided into two distinct "classes" to reflect these differences. Compounds **1**−**8** place the Mn(III), *S* = 2, ions in the body positions of the butterfly metallic core, while the Mn(II), *S* = 5/2, ions occupy the outer wing sites and are described as "Class 1". "Class 2" compounds consist of complexes **9**−**12** and display the reverse arrangement, with the Mn(II) ions in the body positions and the Mn(III) ions occupying the outer wing sites. Using single-crystal X-ray diffraction, magnetic measurements, and DFT calculations, a detailed analysis of the factors that affect the magnetic exchange and, ultimately, the SMM parameters *S* and *D* has been performed, and the results are discussed herein.

EXPERIMENTAL SECTION

General Information. All reactions were carried out under aerobic conditions. Chemicals and solvents were obtained from commercial sources and used without further purification. Elemental analyses (CHN) were carried out by Campbell Microanalytical Laboratory, University of Otago, Dunedin, New Zealand.

Synthesis of Metal Complexes. *$[Mn^{II}_2Mn^{III}_2(hmp)_6(NO_3)_2(H_2O)_2](O_3SC_6H_4CH_3)_2\cdot 2MeCN\cdot 5H_2O$ (**1**).* $Mn(NO_3)_2\cdot 4H_2O$ (0.25 g, 1.0 mmol) was dissolved in MeOH (20 mL), followed by the addition of 2-hydroxymethylpyridine (0.1 mL, 0.5 mmol), *p*-toluenesulfonic acid (0.19 g, 1.0 mmol), and triethylamine (0.28 mL, 2.0 mmol). This resulted in a deep brown solution which was stirred for 3 h. After this time the solvent was removed leaving a brown oil. The oil was redissolved in MeCN, and the solution was left to evaporate slowly. Within 1 week brown crystals of **1** had appeared in an approximate yield of 42% (crystalline product). Anal. Calcd (found) for **1**, $Mn_4C_{54}H_{70}O_{25}N_{10}S_2$: C, 42.03 (41.99); H, 4.57 (4.67); N, 9.08 (8.79).

*$[Mn^{II}_2Mn^{III}_2(hmp)_6(NO_3)_2(O_3SC_6H_4CH_3)_2]\cdot 2MeCN$ (**2**).* The synthesis for **1** (above) was followed, but a larger amount of *p*-toluenesulfonic acid was used (0.76 g, 4.0 mmol). Brown crystals of **2** appeared within 1 week from slow evaporation of the MeCN solution in an approximate yield of 55% (crystalline product). Anal. Calcd (found) for **2**, $Mn_4C_{54}H_{56}O_{18}N_{10}S_2$: C, 45.77 (45.80); H, 3.98 (3.89); N, 9.89 (9.92).

*$[Mn^{II}_2Mn^{III}_2(teaH)_2(teaH_2)_2(iso)_2](NO_3)_2\cdot 2MeOH$ (**3**).* $Mn(NO_3)_2\cdot 4H_2O$ (0.25 g, 1.0 mmol) was dissolved in MeOH (20 mL), followed by addition of triethanolamine (0.13 mL, 0.5 mmol), isonicotinic acid (0.12 g, 1.0 mmol), and triethylamine (0.55 mL, 4.0 mmol), which resulted in a dark brown solution. This was stirred for 3 h, after which time the solvent was removed leaving a brown oil. The oil was redissolved in a CH_2Cl_2:MeOH (9:1) mixture, and upon diffusing diethyl ether into the solution, brown crystals of **3** appeared within 1 day in an approximate yield of 78% (crystalline product). Anal. Calcd (found) for **3**, $Mn_4C_{38}H_{70}O_{24}N_8$: C, 36.72 (36.30); H, 5.68 (5.22); N, 9.02 (8.84).

*$[Mn^{II}_2Mn^{III}_2(teaH)_2(teaH_2)_2(pdca)_2]\cdot 2MeOH\cdot 2H_2O$(**4**).* The synthesis of **3** was followed but 3,4-pyridinedicarboxylic acid (0.16 g, 1.0 mL) was used in place of isonicotinic acid. Brown crystals of **4** could be isolated from diffusion of diethyl ether into the methanolic solution, in approximate yield of 31% (crystalline product). Anal. Calcd (found) for **4**, $Mn_4C_{40}H_{72}O_{24}N_6$: C, 38.72 (38.50); H, 5.85 (5.52); N, 6.77 (6.34).

*$[Mn^{II}_2Mn^{III}_2(teaH)_2(teaH_2)_2(piv)_2](iso)_2\cdot 2MeCN$ (**5**).* $Mn(NO_3)_2\cdot 4H_2O$ (0.12 g, 0.5 mmol) was dissolved in MeOH (20 mL), followed by addition of triethanolamine (0.07 mL, 0.5 mmol), isonicotinic acid (0.03 mL, 0.25 mmol), $[Mn_3O(piv)_6(pyridine)_3]$[7] (0.1 g, 0.1 mmol), and triethylamine (0.28 mL, 2.0 mmol). This resulted in a brown solution. The solution was stirred for 2 h, after which time the solvent was removed leaving a brown oil. The oil was redissolved in a MeCN:MeOH (9:1) mixture, and upon slow evaporation of the solution brown crystals of **5** appeared within 1−2 days in an approximate yield of 54% (crystalline product). Anal. Calcd (found) for **5**, $Mn_4C_{50}H_{86}O_{20}N_8$: C, 44.85 (44.51); H, 6.47 (6.12); N, 4.37 (4.34).

DOI: 10.1021/acs.inorgchem.6b02527
Inorg. Chem. 2017, 56, 1932−1949

[$Mn^{II}_2Mn^{III}_2$(tea-4-nsa)$_2$(4-nsa)$_2$(H_2O)$_2$]·6MeCN (**6**). The synthesis of **3** was followed, but 4-nitrosalicylaldehyde (0.17 g, 1.0 mmol) was used in place of isonicotinic acid. The resulting solution was stirred for 2 h, after which time the solvent was removed to give a brown solid. The solid was redissolved in MeCN, and brown crystals of **6** appeared within 1 week in an approximate yield of 51% (crystalline product). Anal. Calcd (found) for **6**, $Mn_4C_{52}H_{62}O_{24}N_{12}$: C, 37.81 (37.80); H, 5.28 (5.26); N, 10.52 (10.34).

[$Mn^{II}_2Mn^{III}_2$(tea-o-van)$_2$(o-van)$_2$(MeOH)$_2$]·2MeCN (**7**). The synthesis of **3** was followed but *o*-vanillin (0.45 g, 3 mmol) was used in place of isonicotinic acid. The resulting solution was stirred for 2 h, after which time the solvent was removed to give a brown solid. The solid was redissolved in a MeCN:MeOH (1:1) mixture, and upon diffusion of diethyl ether, brown crystals of **7** appeared within 1 week in an approximate yield of 43% (crystalline product). Anal. Calcd (found) for **7**, $Mn_4C_{50}H_{66}O_{20}N_4$: C, 47.55 (47.50); H, 5.27 (5.54); N, 4.44 (4.64).

[$Mn^{II}_2Mn^{III}_2$(tea-o-van)$_2$(teaH$_3$)$_2$](NO$_3$)$_2$·2MeCN (**8**). The synthesis of **7** was followed, but a smaller equivalent of *o*-vanillin (0.15 g, 1 mmol) was added. The resulting solution was stirred for 2 h, after which time the solvent was removed to give a brown solid. The solid was redissolved in MeCN, and upon diffusion of diethyl ether into the solution brown crystals of **8** appeared within 1 week in an approximate yield of 49% (crystalline product). Anal. Calcd (found) for **8**, $Mn_4C_{44}H_{74}O_{24}N_8$: C, 40.07 (40.50); H, 5.66 (5.72); N, 8.50 (8.34).

[$Mn^{II}_2Mn^{III}_2$(teaH)$_2$(O_2CPh)$_4$(acac)$_2$]·MeCN (**10**). $Mn(acac)_3$ (0.36 g, 1 mmol) was dissolved in MeOH (20 mL), followed by addition of triethanolamine (0.13 mL, 1 mmol), benzoic acid (0.1 g, 1.0 mmol), and triethylamine (0.55 mL, 4.0 mmol). This resulted in a brown solution. The solution was heated to reflux and stirred for 2 h, after which time the solvent was removed to give a brown solid. The solid was redissolved in MeCN, and upon slow evaporation of the solution brown, crystals of **10** appeared within 1 week in an approximate yield of 62% (crystalline product). Anal. Calcd (found) for **10**, $Mn_4C_{52}H_{63}O_{18}N_3$: C, 50.46 (50.50); H, 5.13 (5.19); N, 3.40 (3.34).

X-ray Crystallography. X-ray measurements on **1**−**8** and **10** were performed using a Bruker Smart Apex X8 diffractometer with Mo Kα radiation. Data collection and integration were performed within SMART and SAINT+ software programs and corrected for absorption using the Bruker SADABS program. Compounds **1**−**8** and **10** were all solved by direct methods (SHELXS-97)[8] and refined (SHELXL-97)[9] by full-matrix least-squares on all F^2 data.[10] Crystallographic data and refinement parameters for **1**−**8** and **10** are summarized in Table S1. Crystallographic details are available in the Supporting Information (SI) in CIF format. Compounds **1**−**8** and **10** correlate to CCDC Nos. 1483120−1483128, which can be obtained free of charge from the Cambridge Crystallographic Data Center via www.ccdc.cam.ac.uk/data_request/cif.

Magnetic Measurements. The magnetic susceptibility measurements were carried out on a Quantum Design SQUID magnetometer MPMS-XL 7 operating between 1.8 and 300 K for dc-applied fields ranging from 0 to 5 T. Microcrystalline samples were dispersed in Vaseline in order to avoid torquing of the crystallites. The sample mulls were contained in a calibrated gelatin capsule held at the center of a drinking straw that was fixed at the end of the sample rod. Alternating current (ac) susceptibilities were carried out under an oscillating ac field of 3.5 Oe and frequencies ranging from 0.1 to 1500 Hz.

Computational Details. The energies of four spin configurations for **1**−**12** are computed to extract the exchange interactions (see SI for details).[11] The computed spin configurations for **1**−**12** are given in the SI (Table S7). The exchange coupling constants have been calculated using the broken symmetry (BS) approach developed by Noodleman.[12] This method has been employed previously to compute good numerical estimates of exchange interactions in numerous polynuclear complexes.[13] Here all density functional theory (DFT) calculations were performed using the B3LYP functional[14] with Ahlrich's[15] triple-ζ-quality basis set. All calculations have been performed with the Gaussian 09 suite of programs.[16] The PHI[17] program was used for simulating the magnetic susceptibilities. The following spin Hamiltonian was used to calculate the magnetic exchange interactions (see Figure 2).

$$\hat{H} = -[2J_{wb}(S_{Mn1}S_{Mn3} + S_{Mn1}S_{Mn4} + S_{Mn2}S_{Mn3} + S_{Mn2}S_{Mn4}) + 2J_{bb}(S_{Mn1}S_{Mn2}) + 2J_{ww}(S_{Mn3}S_{Mn4})] \quad (1)$$

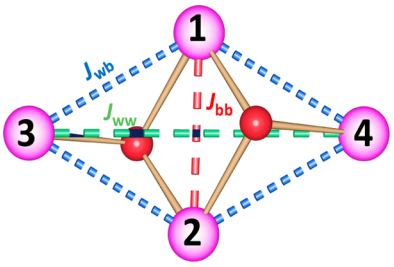

Figure 2. Magnetic exchange pathways in **1**−**12**.

To estimate the error based on the choice of BS solutions, we computed additional broken symmetry solutions and estimated the error as reported earlier.[11,13c] This yielded a negligible error in the range of 0.002−0.008 cm^{-1}.

The zero-field splitting (ZFS) parameter has also been computed for complexes possessing an S_{gs}= 9 ground state using the ORCA program suite.[18] The ZFS parameters are computed using DFT calculations, where the spin−orbit coupling operators are represented by an effective one-electron operator using the spin−orbit mean field (SOMF) method as implemented in ORCA using the B3LYP functional.[18] We used the coupled perturbed (CP) SOC approach to evaluate the spin−orbit contribution to D (D_{SOC}). The spin−spin contribution (D_{SS}) was estimated by using the unrestricted natural orbital approach. Further, to improve the accuracy of the estimated D values, relativistic corrections were performed using the DKH method. Although ab initio CASSCF/PT2 calculations have proven to yield accurate estimates of D values,[19] this methodology cannot be employed here due to the large size of the {Mn_4} complexes.

RESULTS AND DISCUSSION

Synthesis. The targeted syntheses of the {$Mn^{II}_2Mn^{III}_2$} butterfly complexes reported in this work employed the use of two primary ligands. The first, triethanolamine (teaH$_3$), was utilized due to previous literature reports of homometallic 3d and heterometallic 3d−3d and 3d−4f tetranuclear butterfly complexes incorporating this ligand.[1h−j,u,20] A second ligand, which also revealed a propensity for the stabilization of the butterfly metal core topology, is 2-hydroxymethylpyridine (hmpH).[1s,t,6g] Using these two ligands and upon selection of an appropriate coligand it was found that one could easily isolate a range of new mixed-valent Mn(II/III) butterfly compounds. When using hmpH, the coligand in question was *p*-toluenesulfonic acid (**1** and **2**).

Using teaH$_3$, three coligands were employed which were of the carboxylic acid (**3**−**5**) and salicylaldehyde type (**6**−**8**). Interestingly, combination of alcohol and aldehyde groups in basic conditions resulted in the in-situ formation of a hemiacetal functional group and the synthesis of two new ligands. This is observed in complexes **6**−**8**, and it was found that these ligands have not been previously used in the synthesis of polynuclear complexes. The molecular structure of these ligands (tea-4-nsa^{4-} and tea-o-van^{4-}) in their coordinated form are shown in Scheme 1. The ligands are multidentate and will be useful for the syntheses of polynuclear clusters in future studies. The third type of coligand utilized is β-diketonates and resulted in complexes **9**−**12**.

DOI: 10.1021/acs.inorgchem.6b02527
Inorg. Chem. 2017, 56, 1932−1949

Scheme 1. In-Situ Formation of the Coordinated 2-({2-[Bis(2-hydroxyethyl)amino]ethoxy}hydroxymethyl)-4-nitrophenol, tea-4-nsaH_4 (top), and 2-({2-[Bis(2-hydroxyethyl)amino]ethoxy}hydroxymethyl)-6-methoxyphenol, tea-o-vanH_4 (bottom), from teaH_3 and the Appropriate Salicylaldehyde

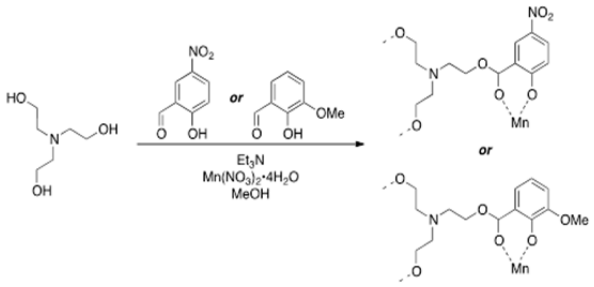

Structural Descriptions. The molecular structures of **1**−**12** were determined by single-crystal X-ray diffraction measurements, which revealed mixed-valent tetranuclear manganese (II/III) complexes. As discussed above, all 12 complexes display a butterfly (or planar-diamond) metallic core arrangement. It was found that the 12 complexes could be divided into two groups denoted as Class 1 and Class 2. The molecular structures of **1** and **9** are shown in Figure 1 as representative examples of Class 1 (top) and Class 2 (bottom). The molecular structure of **2**−**8** and **10**−**12** are given in Figures S1 and S2. The two distinct structural groups are classified with respect to the metal ions. Class 1 compounds, **1**−**8**, reveal that the Mn(III) ions are found in the central body positions of the butterfly, while the Mn(II) ions occupy the outer wing sites (Figure 1a). Class 2 complexes, **9**−**12**, display the reverse oxidation state arrangement (Figure 1b). The oxidation states of the Man ions were easily determined via bond length parameters, structural distortions, and bond valence sum[21] calculations (Table S2). For the sake of brevity, a general description relating to all complexes will be given. It is observed that two μ_3-O atoms bridge the two body Mn ions to an outer Mn wing site in all cases. The O atom is derived from a deprotonated arm of the amine-polyalcohol or the hmp$^-$ ligand. The complexes are further stabilized around the periphery of the core by μ_2-O atoms that bridge a central Mn ion to an outer Mn site. These connections are derived from the amine-polyalcohol ligand or the hmp$^-$ ligands.

The ligands are also found to bridge the Mn(II) and Mn(III) ions (carboxylates) and both bridge and chelate ([β-diketonates]$^-$, [hmp]$^-$, [teaH]$^{2-}$, [p-tol]$^-$), capping the coordination sites. The Mn(III) ions are six coordinate in all complexes, with Jahn−Teller axially distorted octahedral geometries. The Mn(II) ions in complexes **6**, **7**, and **10** are six coordinate with distorted octahedral geometries, while the Mn(II) ions for the remaining nine complexes are seven coordinate, with pentagonal bipyramidal (**1**−**5** and **8**) and capped octahedral (**9**, **11**, and **12**) geometries. We note that the two long Mn−O contacts (~2.6 Å) for compounds **10** and **12** are considered as weak bonds. Tables 1 and S3 contain selected structural parameters and how they relate to the magnetic exchange (J) pathways. From the structural data the first notable observation is the role the coligand plays in influencing the position of the metal ions in the butterfly motif. Class 1 compounds are obtained when using carboxylate and salicylaldehyde coligands with teaH_3 or tosylate coligands with hmpH. However, when β-diketone ligands are used in conjunction with teaH_3, Class 2 complexes are isolated exclusively, even in the presence of a carboxylate ligand, as seen for **10**. A second structural observation reveals that compounds **3** and **4** can conceivably be used as SMM nodes (see magnetic properties, vide infra) in the formation of metal−organic frameworks, due to the noncoordinating 3- and 4-pyridyl groups present (Figure S1b and S1c). Several 1-, 2-, and 3-D networks based on {Mn_4} butterfly complexes have previously been reported.[5]

Table 1. Description of the Bridging Ligands, Average Mn···Mn Distances, Mn−O−Mn Angles, and Related J_{wb} and J_{bb} Pathways in Complexes 1−12

	bridging ligands		d(Mn−Mn) (Å)		Mn−O−Mn angle (deg)	
complex	J_{wb}	J_{bb}	J_{wb}	J_{bb}	J_{wb}	J_{bb}
1	μ_3-O{hmp$^-$} μ_2-O{hmp$^-$}	μ_3-O{hmp$^-$}	3.357, 3.273	3.227	95.9, 100.9, 106.7, 109.7	99.4
2	μ_3-O{hmp$^-$} μ_2-O{hmp$^-$}	μ_3-O{hmp$^-$}	3.412, 3.297	3.259	99.6, 94.6, 108.8, 112.4	100.2
3	μ_3-O{teaH^{2-}} μ_2-O{teaH$_2^-$}	μ_3-O{teaH^{2-}}	3.357, 3.213	3.195	89.8, 102.7, 107.4, 108.9	99.3
4	μ_3-O{teaH^{2-}} μ_2-O{tea H$_2^-$}	μ_3-O{teaH^{2-}}	3.328, 3.234	3.136	91.6, 103.7, 107.7, 106.8	96.4
5	μ_3-O{teaH^{2-}} μ_2-O{teaH$_2^-$}	μ_3-O{teaH^{2-}}	3.320, 3.337	3.152	89.0, 102.9, 104.6, 107.9	97.5
6	μ_3-O{tea-4-nsa $^{3-}$}	μ_3-O{tea-4-nsa^{3-}}	3.335	3.201	93.1, 99.9, 109.2, 112.7	99.9
7	μ_3-O{ tea-o-van $^{3-}$}	μ_3-O{ tea-o-van $^{3-}$}	3.251, 3.268	3.257	93.4, 99.8, 105.7, 108.8	101.1
8	μ_3-O{ tea-o-van $^{3-}$}	μ_3-O{ tea-o-van $^{3-}$}	3.385, 3.388	3.217	92.3, 99.3, 110.0, 113.3	100.1
9	μ_3-O{teaH^{2-}} μ_2-O{paa$^-$}	μ_3-O{teaH^{2-}}	3.306, 3.316	3.628	97.0, 104.4, 97.6, 111.1	100.9
10	μ_3-O{teaH^{2-}}	μ_3-O{teaH^{2-}}	3.215, 3.568	3.444	91.3, 128.4, 110.8	95.7
11	μ_3-O{teaH^{2-}} μ_2-MeO$^-$	μ_3-O{tea^{2-}}	3.272, 3.322	3.625	99.9, 102.7, 94.4, 105.9	102.0
12	μ_3-O{teaH^{2-}} μ_2-O{acac$^-$}	μ_3-O{tea^{2-}}	3.384, 3.390	3.728	93.5, 110.8, 98.0, 115.0	99.9

DOI: 10.1021/acs.inorgchem.6b02527
Inorg. Chem. 2017, 56, 1932−1949

Table 2. Experimentally Fitted and DFT-Calculated Exchange Coupling Constants (J values) for 1−12

	fits to experimental data using PHI;[17] g = 2.0				DFT-calculated J values and spin ground state			
	J (cm^{-1})				J (cm^{-1})			
complex	J_{wb}	J_{bb}	D (cm^{-1})	S_{gs}	J_{wb}	J_{bb}	J_{ww}	S_{gs}
				Class 1				
1	1.87	0.01	−0.33	9	1.24	0.01	−0.01	9
2	1.39	−0.06	−0.37	9	1.37	−0.06	−0.03	9
3	0.66	2.32	−0.34	9	0.37	2.32	−0.08	9
4	0.88	2.06	−0.32	9	0.49	2.06	−0.03	9
5	0.02	2.22	−0.43	9	0.15	2.22	−0.06	9
6	0.47	0.66	−0.32	9	0.31	0.66	−0.03	9
7	−0.42	0.26	−0.01	1	0.24	0.26	−0.02	9
8	−0.46	0.27	0.01	1	0.18	0.27	−0.03	9
				Class 2				
9	0.28	−0.13	−0.35	9	0.47	−0.13	−0.02	9
10	0.05	−0.86	−0.01	1−4	0.32	−0.86	0.08	3
11	1.15	−0.03	−0.33	9	1.08	−0.03	−0.03	9
12	−0.51	0.02	0.003	1	−0.45	0.02	0.001	1

The packing motifs in the crystals of complexes **1**−**12** have been analyzed (see Figure S3−S6). For **1**, **3**, **5**, **10**, and **11**, we observe intermolecular H-bonding interactions which form 1-D chains of {Mn_4} moieties throughout the crystal. For **1** these chains are formed via interactions between the O atoms of the sulfonate groups and the coordinated and noncoordinated water molecules (Figure S3a). For **3**, two types of H-bonded interactions are found. The first is a single H bond between the N atom of the pyridyl ring and a O−H of a $(teaH_2)^-$ ligand. The second reveals three H bonds between multiple groups—a O−H of a $(teaH)^{2-}$ ligand, a solvent MeOH, a nitrate and a O−H of a $(teaH_2)^-$ ligand (Figure S3c). For **5** the H-bonded chains are a result of a O−H $(teaH)^{2-}$ interaction from one {Mn_4} moiety with the N atom of the pyridyl ring of the noncoordinating isonicotinate molecule and the O−H$(teaH_2)^-$ of an adjacent {Mn_4} unit with the carboxylate group of the same isonicotinate ligand (Figure S4b). For **10** intermolecular H bonds are formed between the noncoordinating O−H group of a $(teaH)^{2-}$ ligand and a carboxylate O atom (Figure S6a). For **11** two H bonds are formed between the O−H of a $(teaH)^{2-}$ ligand, a nitrate, and a water molecule (Figure S6b). For complexes **4** and **9** intermolecular H-bonding interactions result in 2-D sheets throughout the crystal (Figure S4a and S5c, respectively). For **2**, **6**, and **7** offset $\pi-\pi$ interactions are found between the hmp ligands (Figure S3b), 4 nsa ligands (Figure S4c), and o-van ligands (Figure S5a), resulting in 1-D chains. Finally, no significant intermolecular interactions are observed for **8** and **12**.

Magnetic Susceptibility Studies. Direct Current Susceptibility and Magnetization Studies. Direct current (dc) magnetic susceptibility measurements were performed on polycrystalline samples of **1**−**12** in the temperature range 2−300 K using an applied magnetic field of 1 T (Figure 3). Isothermal magnetization plots were also recorded in fields between 0 and 5 T (Figure 4). A large variation in the temperature-dependent behavior is observed for the $\chi_M T$ product for some of the compounds **1**−**12**. This observation is due to different exchange parameters and spin state energy levels for each analogue (vide infra), and thus, this family of compounds provides an ideal vehicle for probing the reasons that can cause such differences. If we focus on the experimental plots in Figure 3, we see that compounds **1**, **2**, **3**, **4**, **6**, and **11** show that the $\chi_M T$ values of ∼15.5 cm^3 K mol^{-1} at 300 K are slightly greater than those expected for the uncoupled value for two S = 2 (Mn(III)) and two S = 5/2 (Mn(II)) centers of 14.75 cm^3 K mol^{-1}. On decreasing the temperature, the $\chi_M T$ values increase gradually down to ∼70 K, then more rapidly to reach a sharp maximum (∼33−37 cm^3 K mol^{-1} at ∼11 K), before rapidly decreasing at the lowest temperatures (>10 K). These profiles are indicative of dominant ferromagnetic cluster exchange interactions.

If ferromagnetic coupling is observed for all spins, which would result in a S_{gs} = 9 ground state, then the predicted $\chi_M T$ value of this state is 45 cm^3 K mol^{-1} (g = 2). The observed maxima are, however, found to be lower than this value due to a combination of zero-field splitting, Zeeman level depopulations effects, and intercluster antiferromagnetic coupling, the latter two leading to the rapid decrease below the maximum. The $\chi_M T_{max}$ values are coincidentally close to the value expected for an isolated S = 8 state of 36 cm^3 K mol^{-1}. The magnetization isotherms (Figures 4 and S19−21, SI) are also indicative of zero-field splitting (vide infra). Previous work on {$Mn^{II}_2Mn^{III}_2$} clusters yielded similar $\chi_M T$(T) plots to those found here, arising from a S_{gs} = 9 ground state, often close in energy to higher lying S = 8 and other spin states of lower value.[1a,b,h−r,2,6a−e]

For compounds **5** and **9** the $\chi_M T_{max}$ values are found to be lower, at ∼20−22 cm^3 K mol^{-1}, and even lower for **7** and **8**, with values of ∼16.5 cm^3 K mol^{-1}, suggestive of antiferromagnetic contributions to the exchange coupling. Complexes **10** and **12** reveal the absence of any maximum in $\chi_M T$, with a gradual decrease of $\chi_M T$ between 300 and 50 K, followed by a more rapid decrease down to 2 K, reaching ∼0 cm^3 K mol^{-1}, indicative of antiferromagnetic contributions to the exchange coupling. The $M(H)$ isotherms for **7** and **8** (Figure S20) and **12** (Figure 4) support antiferromagnetic coupling by their linear-like shapes and low M values. They also suggest the presence of nearby nonzero spin states that are thermally populated at progressively higher dc fields.

Fitting of the experimental magnetic data in order to extract the nature and the magnitude of the magnetic exchange interactions (J) within each complex was performed using the PHI program.[17] It is often found that only two J values—J_{bb} and J_{wb} (Figure 2)—are generally reported due to the complications of performing fits of experimental data with multiple J's, and thus, the J_{ww} interaction has been set at zero in

DOI: 10.1021/acs.inorgchem.6b02527
Inorg. Chem. 2017, 56, 1932−1949

Table 3. Literature Reported $\{Mn^{III}_2Mn^{II}_2\}$ Butterfly Complexes with Their Formula, Magnetic Exchange Interactions (J), Ground Spin State S_{gs} Value, and Uniaxial Magnetic Anisotropy Parameter D of the Ground Spin State[a]

molecular formula	J_{bb} (cm^{-1})	J_{wb} (cm^{-1})	S_{gs}	D (cm^{-1})	ref
$[Mn_4O_2(2\text{-Cl-benzoato})_7(bpy)_2]$	−23.2	−4.9	7/2	−0.6	1b
$[Mn_4O_2(2\text{-Br-benzoato})_7(bpy)_2]$	−22.8	−4.7	7/2		1b
$[Mn_4(HX)_4Cl_2(MeOH)_4]\cdot 2Et_2O$	7.7	3.4	9		1c
$[Mn_4(HX)_4Br_2(MeOH)_4]\cdot 2Et_2O$	12.4	3.3	9		1c
$[Mn_4(hmp)_6Br_2(H_2O)_2]Br_2\cdot 4H_2O$	12.7	1.3	9	−0.35	1d
$[Mn_4(hmp)_6(MeCN)_2(H_2O)_2](ClO_4)_4\cdot 2MeCN$	5.9	0.46	9	−0.23	1e
$[Mn_4(hmp)_6(MeCO_2)_2(H_2O)_2](ClO_4)_2\cdot 4H_2O$	5.6	0.54	9	−0.22	1f
$[Mn_4(hmp)_6(PhCO_2)_2(H_2O)_2](ClO_4)_2\cdot 4MeCN\cdot 2H_2O$	5.2	0.9	9	−0.26	1f
$[Mn_4(hmp)_6(MeCO_2)_2](ClO_4)_2\cdot H_2O$	4.5	1.3	9		1f
$[Mn_4(hmp)_6(ClCH_2CO_2)_2](ClO_4)_2\cdot 2H_2O$	4.9	1.1	9		1f
$[Mn_4(hmp)_6(Cl_3CCO_2)_2(H_2O)_2](ClO_4)_2$	3.7	0.6	9		1f
$[Mn_4(hmp)_6(NO_3)_2(MeCN)_2](ClO_4)_2\cdot 2MeCN$	6.3	4.2	9	−0.22	1g
$[Mn_4(hmp)_6(NO_3)_2(NO_3)_2]\cdot MeCN$	9.9	1.0	9	−0.19	1g
$[Mn_4(hmp)_6(acac)_2(MeOH)_4](ClO_4)_2$	5.3	0.77	9	−0.22	1g
$[Mn_4(hmp)_6(H_2O)_2(NO_3)_2](ClO_4)_2\cdot 4H_2O$	9.2	0.85	9	−0.24	1k
$[Mn_4(hmp)_6(N_3)_2](ClO_4)_2$	6.0	0.5	9		1k
$[Mn_4(Hpdm)_6(MeCO_2)_2](ClO_4)_2\cdot 2.5H_2O$	8.7	1.1	9	−0.26	1l
$[Mn_4(hmp)_6(NO_3)_2(dcn)_2]\cdot 2MeCN$	6.8	1.12	9	−0.24	1m
$[Mn_4(hmp)_6(dcn)_2](ClO_4)_2$	6.3	0.7	9		1m
$[Mn_4(hmp)_4(Hpdm)_2(dcn)_2](ClO_4)_2\cdot 2H_2O\cdot 2MeCN$	8.8	0.8	9	−0.28	1m
$[Mn_4(hmp)_4Br_2(MeO)_2(dcn)_2]\cdot 0.5H_2O\cdot 2thf$	7.6	0.9	9		1m
$[Mn_4(Hpdm)_6(MeCO_2)_2](ClO_4)_2\cdot 2MeCN\cdot 2Et_2O$	8.1	0.42	8	−0.24	1n
$[Mn_4(teaH_2)_2(teaH)_2(PhCO_2)_2](PhCO_2)_2\cdot MeCN$	6.6	0.42	9		1o
$[Mn_4(teaH_2)_2(teaH)_2(MeCO_2)_2](MeCO_2)_2\cdot 2H_2O$	6.5	1.7	9		1o
$[Mn_4(teaH_2)_2(teaH)_2(EtCO_2)_2](ClO_4)_2$	10.9	0.2	9		1o
$[\{Mn_4(hmp)_6(MeCN)_2\}\{Pt(mnt)_2\}_4][Pt(mnt)_2]_2$	10.0	0.56	9	−0.21	1q
$[\{Mn_4(hmp)_6(MeCN)_2\}\{Pt(mnt)_2\}_2][Pt(mnt)_2]_2\cdot 2MeCN$	4.3	0.6	9	−0.17	1q
$[Mn_4(hmp)_4(OH)_2Mn(dcn)_6]\cdot 2MeOH\cdot 2thf$	4.9	1.0	9	−0.28	1r
$[Mn_4(hmp)_6(NO_3)_2(H_2O)_2](NO_3)_2\cdot 2.5H_2O$	4.9	0.6	9	−0.24	1s
$[Mn_4(hmp)_6(H_2O)_4](ClO_4)_4\cdot 2H_2O$	3.5	0.39	9		1s
$[Mn_4(hmp)_6(Hhmp)_2](ClO_4)_4\cdot 2MeCN$	0.17	−0.64	1		1s
$[Mn_4(bdea)_2(bdeaH)_2(^tBuCO_2)_4]$	4.7	0.3	9	−0.19	1u
$[Mn_4(bdea)_2(bdeaH)_2(PhCO_2)_4]$	7.7	0.9	9	−0.24	1u
$[Mn_4(teaH_2)_2(teaH)_2(PhCO_2)_2](PhCO_2)_2\cdot 0.7MeCN\cdot 0.3\ EtOH$	8.5	1.8	9	−0.23	1u

[a] H_3X = 2,6-bis(hydroxymethyl)-4-methylphenol. Data reported in K have been converted to cm^{-1} for comparison.

this study. Since there are four J_{wb} and only one J_{bb}, we found that the fit is insensitive to the J_{bb} value. Thus, we fixed the J_{bb} value to that calculated from DFT and extracted the J_{wb} and D parameters from the fit. The results of fitting the experimental data are presented in Table 2, left columns. It is found that the 70−300 K temperature region is the most sensitive to the J values, while at lower temperatures the $\chi_M T$ value is most sensitive to the zero-field splitting and intermolecular cluster coupling. We note that when using DFT all three exchange parameters (eq 1) are explicitly calculated (vide infra). The cross comparison of experimental and calculated (DFT) J values is explained in the theoretical studies section below. Equation 2 is the Hamiltonian used to fit the magnetic data to determine J and D (g = 2.0) for each complex. For comparison, we listed the J, D, and S values for literature reported butterfly $\{Mn^{III}_2Mn^{II}_2\}$ complexes in Table 3.

$$\hat{H} = -[2J_{wb}(S_{Mn1}S_{Mn3} + S_{Mn1}S_{Mn4} + S_{Mn2}S_{Mn3} + S_{Mn2}S_{Mn4}) + 2J_{bb}(S_{Mn1}S_{Mn2})] + DS_z^2 + g\beta H\cdot S \quad (2)$$

The fits obtained for the $\chi_M T$ plots using PHI and eq 2 for Class 1 complexes, **1**−**8**, labeled Fit-x in Figure 3 are generally very good over the 2−300 K range. The J values for the S_{gs} = 9 ground state systems typically have both J_{wb} and J_{bb} positive with $J_{wb} < J_{bb}$. The J values for **3**, **4**, **5**, and **6** are similar to those reported elsewhere for other hmp and triethanolamine analogues.[1j,o,2b,d] The J_{bb} values for **1** and **2**, however, are smaller than those generally observed. Complexes **7** and **8**, with smaller $\chi_M T$ (max) values, gave good fits for negative J_{wb} values and a S_{gs} = 1 ground state.

For Class 2 (**9**−**12**) the best-fit parameters for compound **9** revealed an S_{gs}= 9 ground state which is different to that previously published, viz. $J_{wb}(Mn^{II}\cdots Mn^{III})$ = 5.8 cm^{-1} and $J_{bb}(Mn^{II}\cdots Mn^{II})$ = −8.7 cm^{-1} for g = 2; S_{gs} = 6.[1h] In a similar vein the best-fit parameters for complex **11** are different to those previously published. The parameters are of the same sign, but different in magnitude, viz. J_{wb} = 1.41 cm^{-1}, J_{bb}= −1.38 cm^{-1}, $g(Mn^{III})$ = 1.93 and $g(Mn^{II})$ = 2.00; S_{gs} = 8 with S_{gs} = 7 excited states close in energy to the ground state.[1m] The different parameters for both **9** and **11** found in this study may be attributed to the fact that we have simultaneously fitted both the susceptibility and the magnetization data using eq 2 as well as the fit being insensitive to the J_{bb} values. As the later procedure is more reliable and with the extracted values being in agreement with DFT-estimated parameters, this offers

DOI: 10.1021/acs.inorgchem.6b02527
Inorg. Chem. 2017, 56, 1932−1949

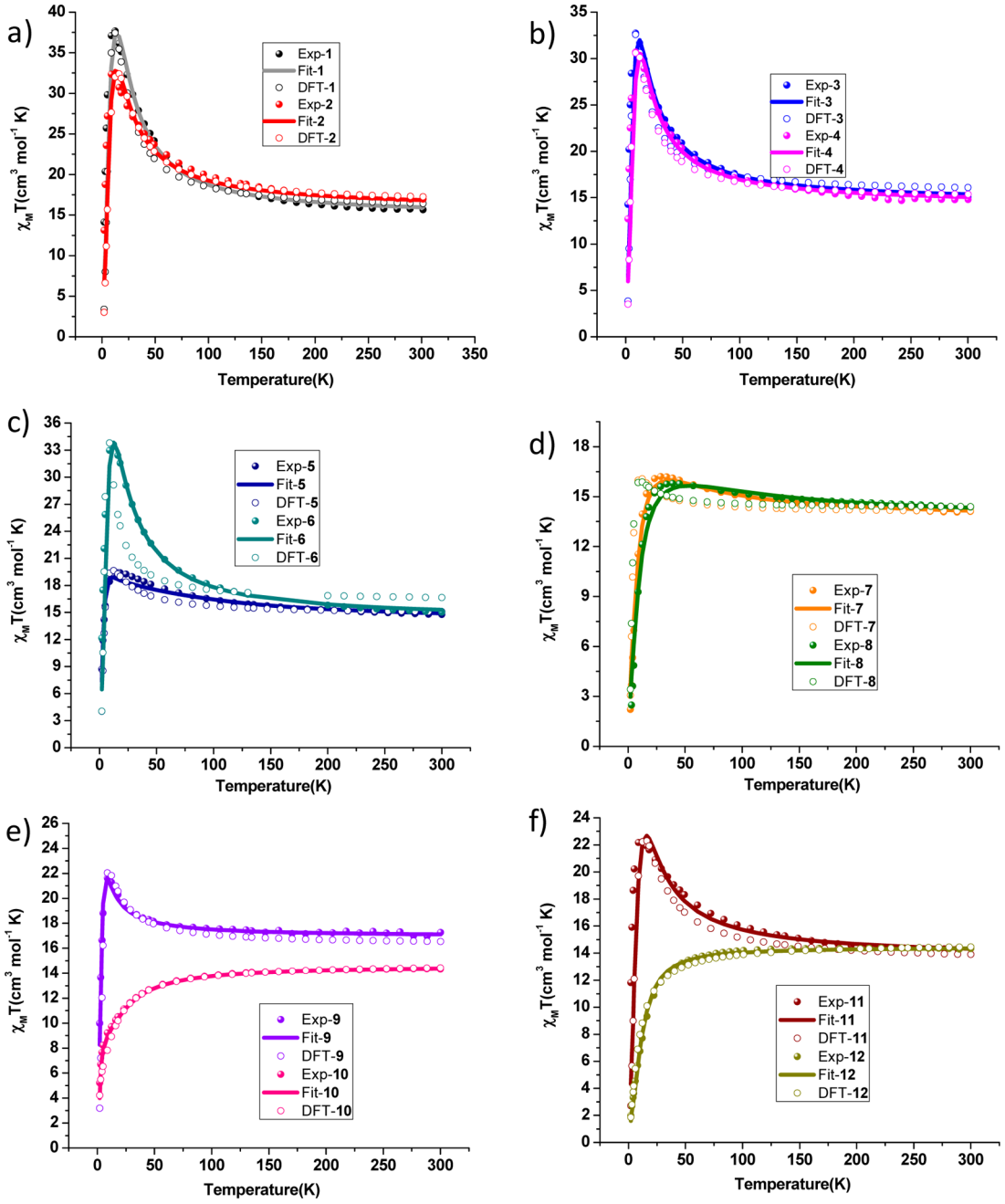

Figure 3. Thermal variation of $\chi_M T$ for (a) **1**–**2**, (b) **3**–**4**, (c) **5**–**6**, (d) **7**–**8**, (e) **9**–**10**, and (f) **11**–**12** down to 2 K at 1 T. Solid lines are fits of the experimental data using the PHI program. Open points are the simulated $\chi_M T$(T) values using DFT-extracted parameters.

confidence on the parameters extracted. Complex **12** shows similar J values to those published with a ground spin state of S_{gs}= 1.[1j] The best fit for the new complex **10** (newly synthesized) reverses the sign of J_{wb} and J_{bb} interactions compared to **12**, resulting in a degenerate ground state situation with the lowest lying spin values ranging from S_{gs} = 1 to S_{gs} = 4.

Magnetization isotherms in the temperature range 2–20 K were measured in order to back up the identification of the ground state and provide information on low-lying excited states, anisotropy, etc. Perusal of Figures 4 and S19–21 shows that fits using eq 2 for **1** and **5** and **2**, **3**, **4**, **6**, and **9**–**11** (SI) are very good for the isotherms with M values in a dc field from 0.5 to 3.5 T. The fits are excellent in the low-temperature region due to the inclusion of the zero-field splitting in the exchange model (see Table 2). Isothermal M vs H fits for the S_{gs} = 1 Class 1 complexes (**7** and **8**) and the S_{gs} = 1 Class 2 complex (**12**) are generally satisfactory, with the zero-field splitting parameter being less important, with the fits yielding negligible values (see Table 2).

The extracted D values using eq 2 for the S_{gs} = 9 complexes are in the range from −0.32 to −0.43 cm^{-1}, which are similar to the literature reported D values of other manganese butterfly complexes[5] (see Table 2), offering confidence on the parameters extracted.

Alternating Current Susceptibility Studies. Alternating current (ac) susceptibility measurements were performed to determine if **1**–**12** display slow magnetization reversal. It was found that slow magnetization relaxation is indeed observed for

DOI: 10.1021/acs.inorgchem.6b02527
Inorg. Chem. 2017, 56, 1932–1949

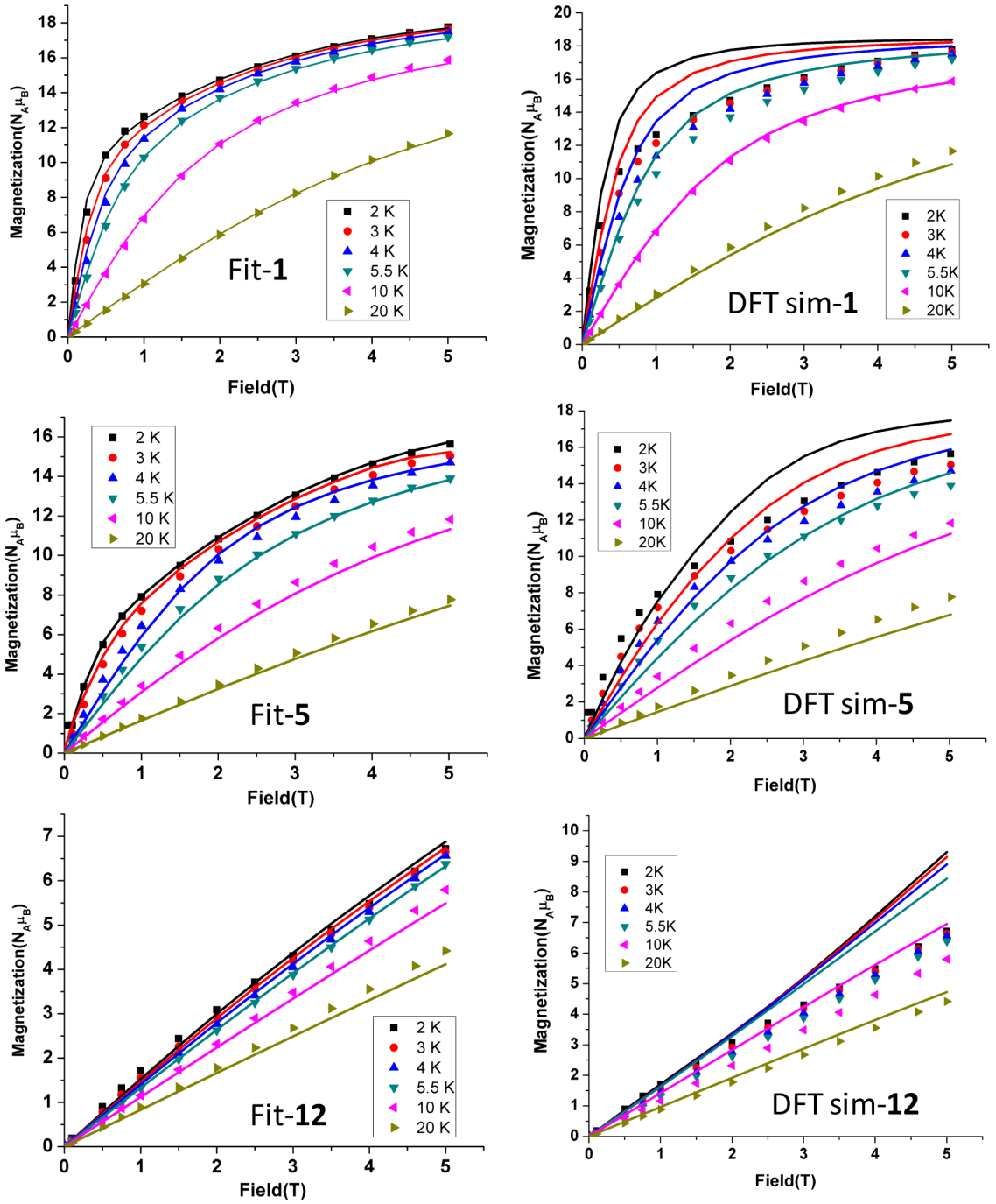

Figure 4. *M* vs *H* isotherms for (top) **1**, (center) **5**, and (bottom) **12** at temperatures of 2, 3, 4, 5.5, 10, and 20 K. Colored shapes are experimental data, colored lines are fits of the experimental data (left), and simulation with the DFT-computed *J* parameters (right).

all complexes, except for **10** and **12**, as determined from the appearance of frequency- and temperature-dependent out-of-phase susceptibility (χ_M'') signals. The χ_M'' vs T plots of compounds **2** and **6** are shown in Figure 5 as representative examples, with plots of the remaining complexes shown in Figures S8–S14, along with the in-phase χ_M' vs T and χ_M' vs frequency plots. The relaxation times (τ) for **1**, **2**, **3**, **6**, and **9** are temperature dependent and when plotted as ln(τ) versus 1/T display a linear relationship. Fitting the data to the Arrhenius law [$\tau = \tau_o \exp(U_{eff}/k_BT)$] yielded anisotropy barriers (U_{eff}) and pre-exponential factors (τ_0) of 13.1 cm^{-1} and 1.5×10^{-8} s (**1**), 11.7 cm^{-1} and 3.6×10^{-8} s (**2**), 16.6 cm^{-1} and 2.6×10^{-10} s (**3**), 16.8 cm^{-1} and 1.6×10^{-8} s (**6**), and 11.8 cm^{-1} and 3.9×10^{-8} s (**9**) (see Figure S15). For complexes **5**, **7**, **8**, and **11** no maxima are observed above 1.8 K, suggesting smaller anisotropy barriers and faster relaxation times. For **7** and **8**, while slow magnetization relaxation behavior is observed, the ground state S value could not be uniquely determined (reported as S = 1, in Table 2) as saturation in the magnetization is not observed. This indicates there are several close-lying excited states as has been witnessed in several Mn clusters.[13h] Indeed, from the dc susceptibility fitting analysis it is found that excited states of values S = 0–6 and S = 0–5 remain populated even at 2 K for **7** and **8**, respectively. This would lead to the conclusion that the slow relaxation originates from populated excited state(s), which is backed up by the small

DOI: 10.1021/acs.inorgchem.6b02527
Inorg. Chem. 2017, 56, 1932–1949

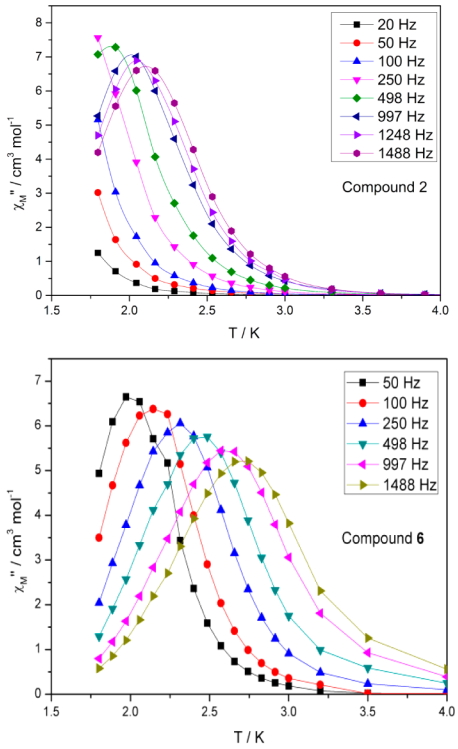

Figure 5. Temperature dependence of χ_M'' for **2** (top) and **6** (bottom) with H_{ac} = 3.5 Oe and H_{dc} = 0 Oe.

χ_M''/χ_M' ratio of 0.03. The absence of slow magnetic relaxation for **10** and **12** is due to the isolated S = 1 ground state for **12** and the small spin and anisotropy found for **10**.

To understand the origin of the contrasting magnetic properties for these structurally related $\{Mn^{II}_2Mn^{III}_2\}$ butterfly complexes, we have undertaken a detailed DFT study performing calculations using the B3LYP/TZV setup to estimate the exchange interactions and the zero-field splitting parameters.

Theoretical Studies. Magnetic Exchange Coupling Parameter (J). Three exchange coupling constants are determined by DFT and are calculated using the B3LYP hybrid functional. The exchange topology used to calculate and simulate the J values is shown in Figure 2. We have set three goals that the DFT calculations can help elucidate: (1) to study the magnetic properties of the $\{Mn^{II}_2Mn^{III}_2\}$ butterfly complexes by calculating the exchange coupling constants (J), (2) to develop magneto-structural correlations that will help us understand which structural parameters affect the J values, and (3) to calculate the zero-field splitting (ZFS) parameter (D) to assess the nature of D in determining the slow magnetization relaxation behavior of these complexes.

To gain confidence in the computed J values, cross comparison of the DFT J parameters with the fitted J values obtained from the experimental magnetic data will be discussed, followed by the computed susceptibility data. This will then be followed by an analysis of geometrical correlation to the observed J values.

The experimentally fitted and DFT-computed J values for complexes **1**−**12** are given in Table 2. It is found that, in general, the sign of the magnetic exchange can be reproduced between the two techniques. In many cases, however, the magnitude of the various exchange parameters differ, the results of which are summarized below.

As stated above, the J_{bb} parameter is fixed to the DFT-calculated value. Thus, only J_{wb} is variable in the experimental data fit. For complexes **1**−**4** (Class 1) it is found that the nature of the exchange interaction as determined from both the experimentally fitted parameters and the DFT-calculated values are in agreement. The analysis reveals ferromagnetic magnetic exchange coupling for both J_{wb} and J_{bb} interactions, except for **2**, where DFT predicts an antiferromagnetic interaction for J_{bb} (Table 2). The magnitude of the ferromagnetic J_{wb} exchange is found to be slightly larger for the experimentally determined parameters compared to DFT. It was also determined from DFT that the J_{ww} interaction is very weak and antiferromagnetic in all cases and can thus be ignored for fitting the magnetic data.

For **5**−**8** (Class 1), the parameters derived from the experimental data and DFT yield the same sign of J_{wb} for **5** and **6** but differ for **7** and **8** (Table 2). The experimentally determined J_{wb} parameters are ferromagnetic for **5** and **6** and antiferromagnetic for **7** and **8**. The DFT calculations predict a ferromagnetic J_{wb} interaction for **5**−**8**. In all cases, the J_{bb} interaction is ferromagnetic. As with **1**−**4**, DFT predicts that the J_{ww} interaction is negligible and antiferromagnetic.

For **9**−**12** (Class 2), the nature of the magnetic interaction is again in good agreement between the fitted and the DFT parameters. The J_{wb} interaction is found to be ferromagnetic, while J_{bb} is antiferromagnetic for **9**−**11**. This trend is reversed for **12**.

The temperature dependence of $\chi_M T$ for the DFT-calculated J values provides satisfactory fits to the experimental data for **1**−**4** (see Figures 3a, 3b, and S16), **5**−**8** (see Figures 3c, 3d, and S17), and **9**−**12** (see Figures 3e, 3f, and S18). The DFT-calculated magnetization data also afforded reasonable fits to the experimental M vs H data for the majority of complexes but with poor agreement at 2, 3, and 4 K and at intermediate field values. The fits using PHI and eq 2 are superior (see Figure 4 top (**1**), center (**5**), and bottom (**12**) and Figures S19−S21 for **2**−**4** and **6**−**11**).[1j] At lower temperatures, the anisotropic contributions are likely to play a role, and this has not been included in the DFT magnetization simulation.

Analysis of J_{bb} for 1−12. This interaction, for all complexes, mediates through two alkoxo bridges and occurs between two Mn^{III} centers in **1**−**8** and two Mn^{II} centers in **9**−**12**. The interaction is found to be ferromagnetic from the DFT calculations (with the exception of **2**) for Class 1 complexes, while it is antiferromagnetic in Class 2 (with the exception of **12**). The magnitude of the DFT-calculated J_{bb} parameter in Class 1 varies from +2.32 to −0.06 cm^{-1}. Table 1 lists all of the geometrical parameters associated with **1**−**12**, and these are used to determine the reason behind the variation in the J values. From previous work and by developing magneto-structural correlations on various $Mn^{III}(OR)_2Mn^{III}$ dimers,[22] it was concluded that the orientation of the Jahn−Teller axes plays a pivotal role in determining the sign and strength of the J parameter. For **1**−**8** the interaction falls in the type II class, type II being defined in the dimer study mentioned above,[22] and as expected the J values are found to be weakly ferromagnetic or antiferromagnetic.[22] This is essentially due to smaller overlap between the magnetic orbitals due to the parallel orientation of the Jahn−Teller axes (see Figure 6a for a schematic illustration of the interaction expected for this building unit). The computed J values are found to be correlated to the Mn^{III}−Mn^{III} distance, with shorter distances yielding ferromagnetic coupling and longer distances yielding weaker ferromagnetic or

DOI: 10.1021/acs.inorgchem.6b02527
Inorg. Chem. 2017, 56, 1932−1949

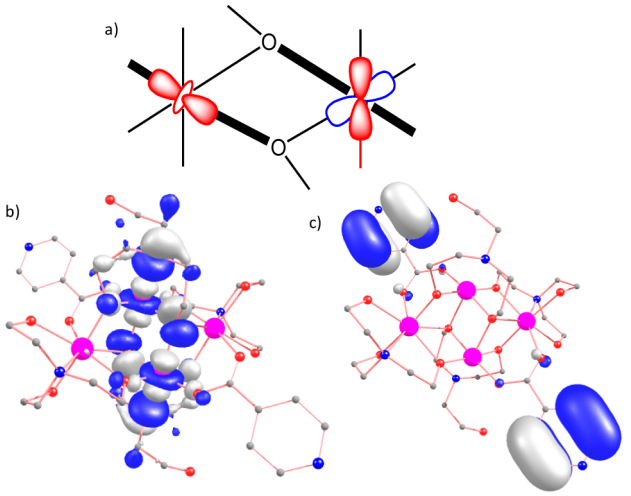

Figure 6. (a) Schematic illustration of the interaction in type II complexes.[22] Bold lines along the μ-O bonds represent the JT axes that visualizes the parallel orientation. (b) Singly occupied molecular orbital (SOMO) of the α electron in **3**. (c) SOMO of the β electron in **3**. White and blue colors represent positive and negative sign.

even antiferromagnetic interactions. This trend is clearly visible from Table 1, with shorter Mn^{III}–Mn^{III} distances revealing ferromagnetic interactions. However, the variation in the Mn^{III}–Mn^{III} distances are also correlated to the variation in the Mn^{III}–O distance and Mn^{III}–O–Mn^{III} angles. Correlations developed earlier suggest that these are the two key parameters influencing the magnitude of J in type II dimers.[22]

For complexes **9**–**12**, the Mn^{II}–Mn^{II} distances are also found to correlate to the magnitude of the J value, as the distance increases the J value is also found to increase, becoming less antiferromagnetic, and in the case of **12**, which has the largest Mn^{II}–Mn^{II} distance, the interaction is weakly ferromagnetic. Besides the Mn^{II}–Mn^{II} distance there is also a correlation with the Mn^{II}–O–Mn^{II} angle,[13h] with an increasing angle resulting in a decrease in the magnitude of antiferromagnetic contribution to the net J value.

Analysis of J_{wb} for Complexes 1–12. This interaction describes the magnetic exchange between a Mn^{III} and a Mn^{II} ion and is mediated by two alkoxo bridges for all complexes. The magnitude of J from the DFT calculations is found to vary from +1.37 to −0.45 cm^{-1}. Analysis of the orbital interaction reveals that the Mn(III)-d_{z^2}|Mn(II)-d_{z^2} overlap controls the sign and magnitude of the J parameter. For all complexes, except for **12**, the d_{z2}–d_{z2} orbitals are parallel, thus avoiding significant orbital overlap, leading to the absence of a significant antiferromagnetic contribution to the J parameter. For complex **12**, on the other hand, due to the variation of structure and the orientation of the Jahn–Teller axes, head-to-head Mn(III)-d_{z^2}|Mn(II)-d_{z^2} overlap is detected leading to antiferromagnetic coupling (see Figure S22 in SI). The variation in the magnitude of the ferromagnetic J's are found to correlate to the Mn–O–Mn angles and the Mn–O distances.

Spin Ground State and Spin Density Analysis of 1–12. The experimentally fitted and DFT-computed J values yield an S = 9 ground state (see Figure 7a) for complexes **1**–**6**, **9**, and **11** (see Table 2). The ground state spin density plot for S = 9 (DFT calculated) is shown in Figure 8a. In all complexes, spin delocalization is observed for the Mn(II) ions (spin density of ~4.82), whereas the Mn(III) ions display a mixture of spin delocalization and polarization (~3.86). From the delocalization, a significant spin density of 0.05 is found on the central μ_3-O atoms that bridge the two body ions to the wing ions, while the outer μ_2-O atoms bridging a body to a wing site gain a spin density of 0.03.

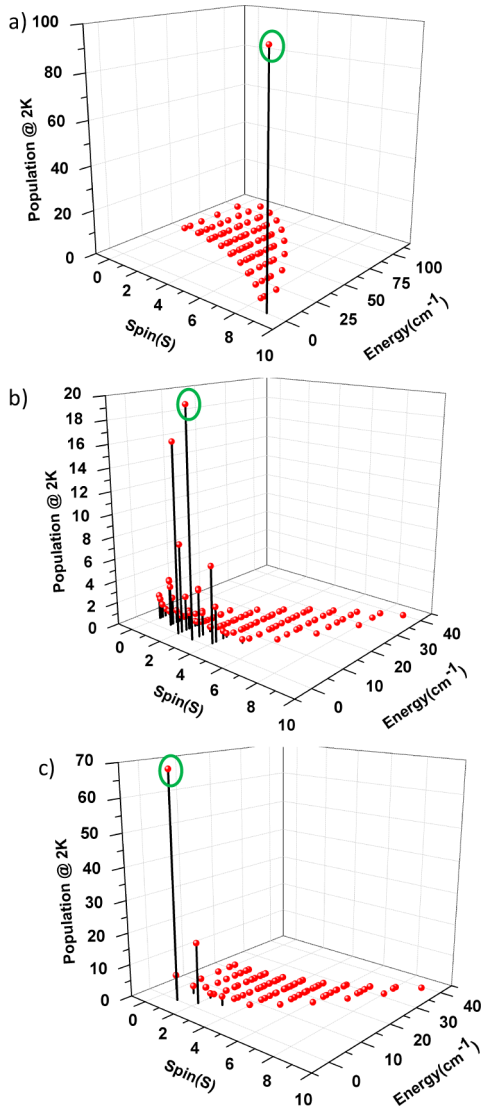

Figure 7. Eigenvalue plots for (a) **1** (a similar diagram is applicable for complexes **2**–**9** and **11**), (b) **10**, and (c) **12** (spin ground state is highlighted).

For complexes **7** and **8**, DFT-computed J values suggest an S = 9 ground state; however, the same value could not be unambiguously determined from the experimental data. As the exchange interactions are very weak for these complexes, this leads to several nested spin states (nearly 10 spin states lie within an energy window of 5 cm^{-1}).

For complex **10**, the experimental J values predict that spin states of S = 1–4 are lowest in energy, while the DFT-computed J values yield an S = 3 ground state (see Figure 7b). The spin state (S = 4) near to the ground state for complex **10** (DFT) is achieved when one body Mn(II) ion has a "spin-down" configuration, while the other Mn centers are "spin-up". This is realized as the dominant interaction predicted in **10** is J_{bb}, which is antiferromagnetic (−0.88 cm^{-1}), whereas the J_{wb} interactions is weaker and computed to be ferromagnetic (0.32 cm^{-1}). This spin configuration should lead to an overall S = 4 value for the ground state. However, due to the competing

DOI: 10.1021/acs.inorgchem.6b02527
Inorg. Chem. 2017, 56, 1932–1949

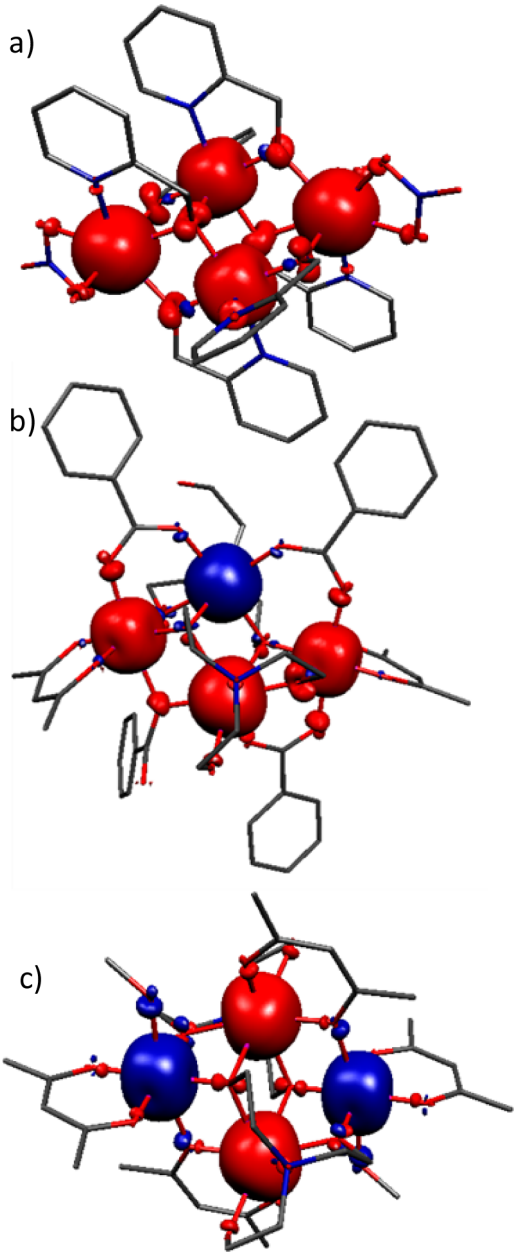

Figure 8. Spin density plots of complexes (a) **1**, (b) **10**, and (c) **12**. Red and blue colors represent positive and negative spin densities.

nature of the interactions, the calculation revealed an S = 3 ground state. The spin density plot for S = 4 is shown in Figure 8b, and the mechanism of delocalization is similar to that discussed above.

For complex **12** the experimental fit and the computed J values yield an S = 1 ground state (see Figure 7c). The spin ground state is attained when two wing Mn(III) ions are "spin-down", while the body Mn(II) ions are "spin-up". The dominant interaction predicted in complex **12** is the antiferromagnetic J_{wb} (-0.45 cm^{-1}) pathway. Even though J_{bb} and J_{ww} are ferromagnetic, they are negligible in magnitude (0.02 and 0.01 cm^{-1}) and do not play a role in determining the ground state. The ground state spin density plot for S = 1 is shown in Figure 8c. Here the spin-down Mn(III) ions have a spin density of ∼−3.84. The central bridging μ_3-O atoms and μ_2-O display a spin density of 0.01 and −0.01, respectively.

Magnetic Anisotropy. Following on from the determination of the magnetic exchange parameters and spin values, we then proceeded to calculate the cluster g and D parameters using DFT for the complexes possessing an S = 9 ground state (**1**−**9** and **11**). Although ab initio CASSCF calculations have proven to give good numerical estimates of cluster D values, this procedure cannot be employed to obtain ground state anisotropy for large clusters such as the ones studied here.[19c−e,23] Thus, the calculated D values are underestimated compared to the extracted D values from the experimental data. The computed isotropic g values for **1**−**9** and **11** are given in Table 4, along with the ZFS parameters (D). The computed g tensors are found to be isotropic for the S = 9 ground state for **1**−**9** and **11**, and the calculations reveal a negative sign of D for these complexes. The different contributions to the net D parameter are also summarized in Table 4. It is observed that D_{soc} (spin−orbit) makes a significant contribution to the net ZFS parameter compared to the D_{SS} (spin−spin) contribution in the cases of largest D. This is found for **2**, **3**, **4**, and **6**. The other complexes reveal a smaller negative ZFS parameter, with equal contributions from D_{soc} and D_{SS}. The different contribution of D_{soc} is listed in Table S4. The largest contributions to the D_{soc} component for complexes **2**, **3**, **4**, and **6** are found to arise from spin-flip excitations α(SOMO, singly occupied molecular orbital) → β(SOMO) excitations as well as a spin-conserving excitations (SOMO → VMO (virtual molecular orbital). Here the $\alpha \rightarrow \beta$ spin-flip excitations are more prominent and contribute in the range of 70−80% to the total D value in **2**, **3**, **4**, and **6**. A closer look at the molecular orbitals reveals that this transition corresponds to metal (d_{z2} orbitals of Mn^{III}, See Figure 6b) low-lying π^* orbitals attached to the bridging ligands, e.g., in complex **3** it corresponds to π^* orbitals of the isonicotinic acid, see Figure 6c). The absence of such substituents leads to high-energy α(SOMO) → β-(SOMO) excitations and therefore smaller contributions to the total D parameter (for example, in complex **5**). This invariably suggests that the electron-donating and -withdrawing substituent's influence not only the magnitude of the J values but also the magnetic anisotropy by offering lower energy excitations and hence enhanced D_{soc} contributions.

Table 4. B3LYP-Computed D, E/D, g Values, along with the Different Contributions to the Computed ZFS Parameter for 1−9 and 12

	DFT-calculated values				
complex	D (cm^{-1})	E/D	D_{SOC} (cm^{-1})	D_{SS} (cm^{-1})	g (isotropic)
1	−0.062	0.219	−0.033	−0.029	2.002
2	−0.152	0.311	−0.122	−0.030	2.001
3	−0.19	0.079	−0.159	−0.031	2.001
4	−0.183	0.293	−0.166	−0.017	2.002
5	−0.067	0.161	−0.035	−0.032	2.002
6	−0.191	0.064	−0.161	−0.03	2.001
7	−0.051	0.201	−0.031	−0.02	2.002
8	−0.065	0.149	−0.034	−0.031	2.002
9	−0.073	0.113	−0.037	−0.036	2.001
11	−0.069	0.211	−0.038	−0.031	2.002

Magneto-Structural Correlations. We developed magneto-structural correlations for complexes **3** (Class 1) and **9** (Class 2) to rationalize the structural parameters that affect the magnetic exchange interactions within these complexes. Correlations for five structural parameters which can affect

DOI: 10.1021/acs.inorgchem.6b02527
Inorg. Chem. 2017, 56, 1932−1949

the exchange interaction have been developed (see Figure 9): (1) Mn_b–O bond distance, (2) Mn_w–O bond distance, (3) Mn_b–O–Mn_b angle (α), (4) Mn_b–O–Mn_b–O dihedral angle (γ), and (5) out-of-plane shift of the Mn_w atoms (β).[24]

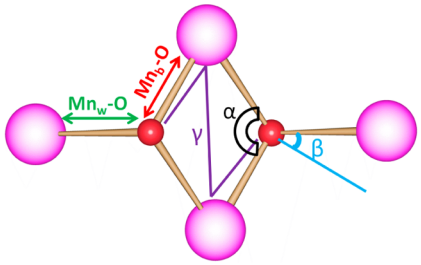

Figure 9. Structural parameters that can affect the exchange interaction.

Class 1. Mn_b–O Distance Correlation. This correlation is developed by varying the Mn_b–O distances from 1.7 to 2.3 Å. While J_{ww} is found to be unaltered, the J_{bb} and J_{wb} values are affected with longer distances yielding less antiferromagnetic J values. It is found that the body–body interaction (J_{bb}) depends mainly on the Mn_b–O distance (from −18.8 to 0.8 cm^{-1} between 1.7 and 2.5 Å). For shorter Mn_b–O distances, the J_{bb} interaction gives rise to strong antiferromagnetic behavior (see Figure 10a). As the Mn_b–O distance is correlated to the d_{z2} orbital interaction, shortening this distance will enhance the overlap with both the Mn^{II} and the Mn^{III} ions leading to antiferromagnetic coupling. The wing–body (J_{wb}) interaction is marginally affected by the Mn_b–O distance parameter (from −1.39 to 1.75 cm^{-1}).

Overlapping the experimentally determined fits (J_{bb} and J_{wb}) on the computed correlation reveals, however, little variation in the Mn_b–O parameter among the family of structures studied here and reported earlier. However, we would like to note that the correlation is developed by fixing all geometric parameters to that of complex **3**, except for varying the Mn_b–O distances, while experimental structures reflect changes on all structural parameters.

Mn_w–O Distance Correlation. This correlation is developed by varying the Mn_w–O distances from 1.9 to 2.7 Å (see Figure 10b). While J_{ww} and J_{bb} are found to be nearly unaltered, the J_{wb} parameter is affected, with longer distances yielding less ferromagnetic J values (from +7 to −1 cm^{-1}). Overlapping the experimentally determined fits on the computed correlation reveal some Mn_w–O structural variation, suggesting flexibility in this parameter across the structures studied.

Mn_b–O–Mn_b Angle Correlation. This angular correlation is developed by varying the Mn_b–O–Mn_b angle from 80° to 120°. For the J_{bb} and J_{wb} interaction, the J values vary from −28.9 to 2.62 cm^{-1} and from −0.8 to 0.9 cm^{-1}, respectively, as the angle is changed. At smaller Mn_b–O–Mn_b angles, the J_{bb} interaction gives rise to strong antiferromagnetic behavior (see Figure 10c). As the angle increases the interaction becomes less antiferromagnetic due to the diminishing overlap between the magnetic orbitals, leading to a smaller antiferromagnetic contribution. The J_{ww} parameter is found to be insensitive to the Mn–O–Mn angle.

Mn_b–O–Mn_b–O Angle (γ). This correlation is developed by varying the γ angle from 0° to 35°. For small Mn_b–O–Mn_b–O angles (0–10°), the J_{bb}, J_{wb}, and J_{ww} interactions are ferromagnetic. It is found that all three J values are sensitive to the angle such that larger γ values yield increasingly antiferromagnetic J_{wb} and J_{bb} and increasingly ferromagnetic J_{ww} interactions (see Figure 10d).

Mn_w–O–O Angle (β). This parameter does not influence J_{bb} or J_{ww}; however, it influences the J_{wb} parameter. At angles > 82° the interaction becomes increasingly ferromagnetic before plateauing above 100°.

From the correlation, it is found that the wing–wing interaction (J_{ww}) is not affected by geometrical changes and remains weak for the whole range of investigated geometrical parameters, except for the γ parameter where it is found to vary. From the data we can therefore conclude that the magnetic exchange interactions (J_{bb} and J_{wb}) of Class 1 complexes are predominantly affected by the Mn_b–O bond distance and the Mn_b–O–Mn_b bond angle, whereas the Mn_w–O bond distance, the dihedral Mn_b–O–Mn_b–O angle (γ), and the out of shift plane parameters play a minor role in influencing the magnetic exchange parameters (Figure 10b and 10d).

Class 2. Similar magneto-structural correlations are also developed for complex **9** and indicate that the body–body interaction (J_{bb}) depends mainly on the Mn_b–O–Mn_b angle (from −6.62 to −0.13 cm^{-1} between 80° and 120°). At the largest and smallest Mn_b–O–Mn_b angles, the J_{bb} interaction gives rise to the strongest antiferromagnetic value (see Figure 11c). The J_{wb} and J_{ww} interactions are not affected by the Mn_b–O–Mn_b angle. The wing–body interaction (J_{wb}) is affected by the Mn_w–O bond distance and the dihedral Mn_b–O–Mn_b–O angle (γ) (see Figure 11b and 11d). At larger Mn_b–O–Mn_b–O angles, the J_{wb} interaction shows antiferromagnetic coupling, and the J_{ww} shows moderate ferromagnetic behavior. Comparatively, the other structural parameters Mn_b–O and the out of plane shift parameter (see Figure 11a and 11e) do not affect the J_{wb} values as much as the Mn_b–O–Mn_b bond angle, the Mn_w–O bond distance, and the dihedral Mn_b–O–Mn_b–O angle, Table 5.

To gain further insight into the correlations developed for complexes **3** and **9**, we analyzed the structural parameters and the corresponding J values observed for other complexes. In Class 1, the J_{bb} parameter mainly varies by changing the Mn_b–O distance and the Mn_b–O–Mn_b angle. The Mn_b–O distance and the Mn_b–O–Mn_b angle for Class 1 complexes are ∼2.1 Å and 96.3–101.1°, respectively. As the Mn_b–O distance is similar for all complexes this suggests that this parameter is not causing the differences found in the J analysis for Class 1 compounds. The variation is therefore primarily due to the changing Mn_b–O–Mn_b angle. The correlations suggest moderate ferromagnetic behavior for J_{bb} for these structural parameters, which is in broad agreement with the extracted experimental J values.

The J_{wb} interaction on the other hand is expected to be influenced by Mn_b–O and Mn_w–O distances and the Mn_b–O–Mn_b–O dihedral angle (γ). The developed correlation revealed a stronger dependence of J_{wb} on the Mn_w–O distance and the Mn–O–Mn_b–O dihedral angle. However, these two parameters are nearly constant for all structures reported for Class I structures (see experimental points in Figure 10). On the other hand, a moderate dependence on the J parameter is noted for Mn_b–O–Mn_b bond angles. As this parameter is found to vary among the structures studied, this parameter rationalizes the observed variation in the J_{wb} values. The correlations also show that the wing–wing interaction (J_{ww}) is not affected significantly by any of the structural parameters,

DOI: 10.1021/acs.inorgchem.6b02527
Inorg. Chem. 2017, 56, 1932–1949

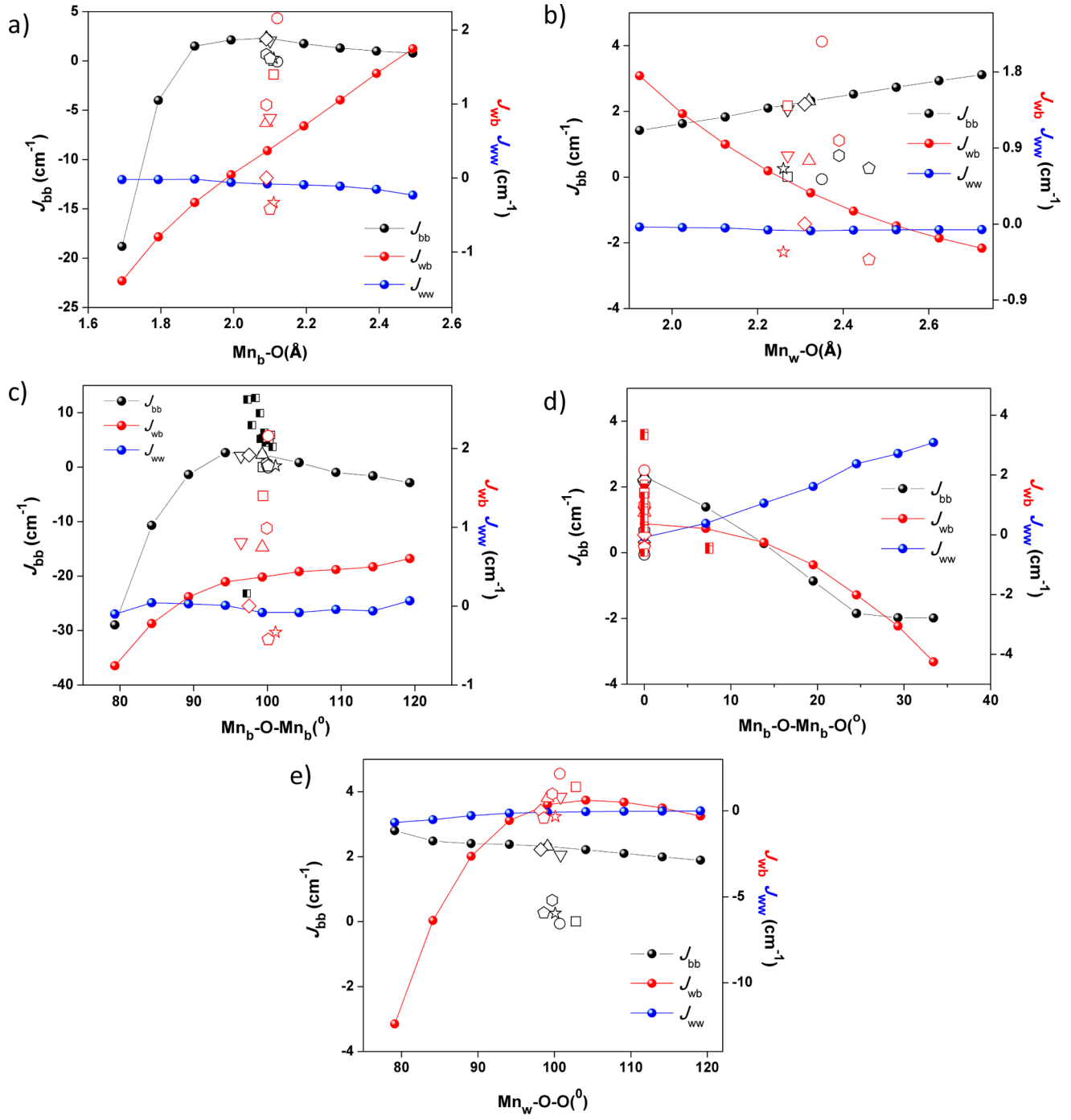

Figure 10. Structural parameters that affect the exchange coupling constants (a) Mn_b−O bond distance, (b) Mn_w−O bond distance, (c) Mn_b−O−Mn_b bond angle, (d) dihedral Mn_b−O−Mn_b−O angle, and (e) out-of-plane shift of the Mn_w atoms. Black (J_{bb}) and red (J_{wb}) open symbols are experimental J values of **1** (squares), **2** (circles), **3** (triangles), **4** (upside down triangles), **5** (diamonds), **6** (hexagons), **7** (stars), and **8** (pentagons). Half shaded squares in c and d are J_{bb} and J_{wb} values of reported $\{Mn^{II}_2Mn^{III}_2\}$ complexes, respectively (Class 1).

revealing very weak exchange interactions, which is in excellent agreement with the calculated J_{ww} for all Class 1 complexes.

In Class 2, the structural parameter which is found to affect the J_{bb} value is the Mn_b−O−Mn_b angle, which ranges from 95° to 102° for **9**−**12**. Our correlation suggests that antiferromagnetic behavior is expected and will be greater at larger and smaller angles (boundaries). This is in good agreement with the calculated J_{bb} values for all Class 2 complexes, except **12**, which is found at the optimum angle between the smaller and the larger angle resulting in ferromagnetic behavior. The J_{wb} interaction is affected by all parameters, except the Mn_b−O distance. It is found, however, that the structural parameters do not vary significantly, and the weak ferromagnetic exchange (weak antiferromagnetic for **12**) extracted from the fits agrees nicely with the correlations.

The J_{ww} interactions are affected by the dihedral angle (γ), which is in the range of 0−2.1°. The dihedral angle correlation suggests that the wing−wing interaction (J_{ww}) shows only a weak exchange interaction up to 2.1°, which is in excellent agreement with the calculated J_{ww} for all Class 2 complexes.

DOI: 10.1021/acs.inorgchem.6b02527
Inorg. Chem. 2017, 56, 1932−1949

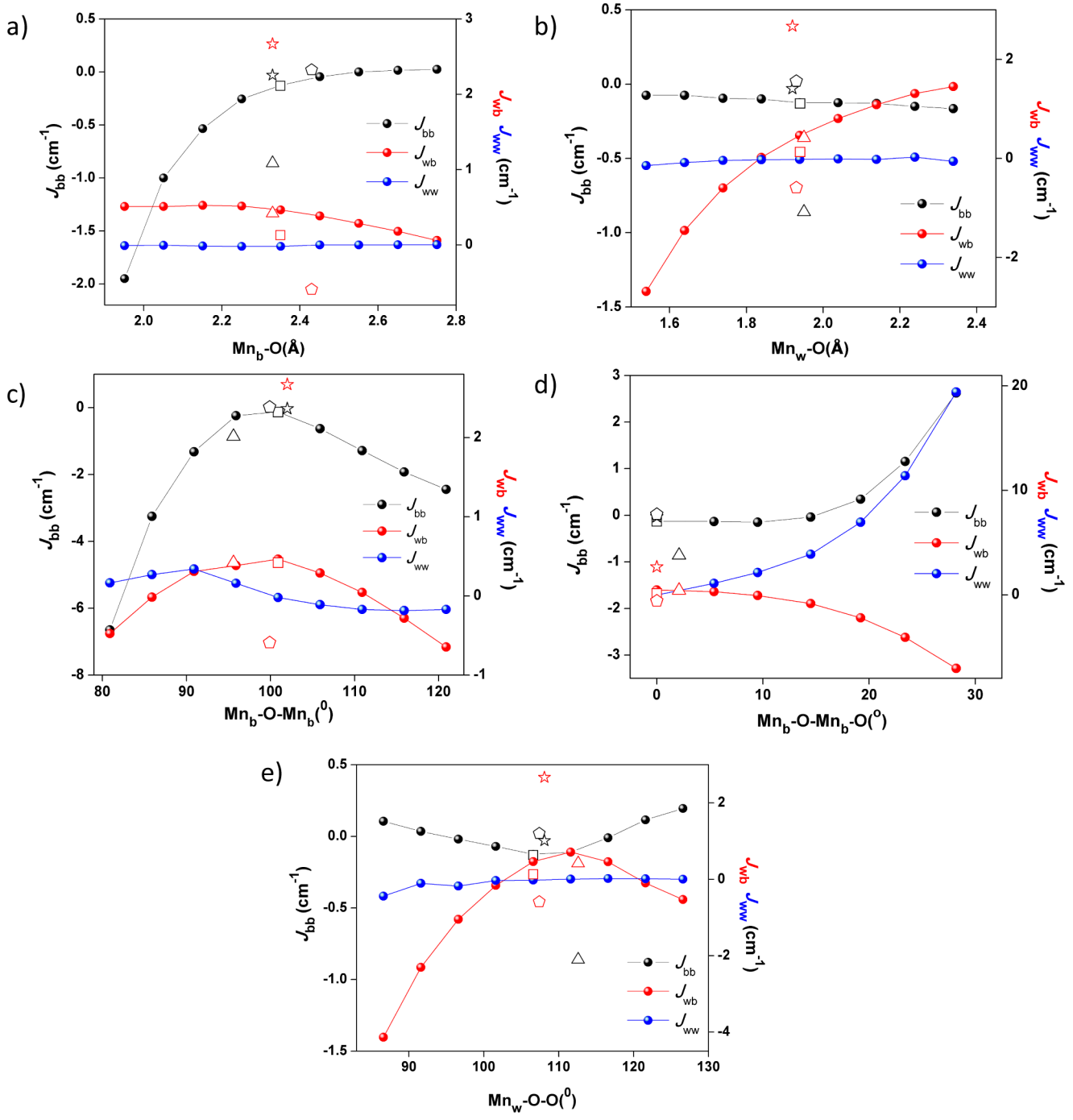

Figure 11. Structural parameters that affect the exchange coupling constants with the (a) Mn_b−O bond distance, (b) Mn_w−O bond distance, (c) Mn_b−O−Mn_b bond angle, (d) dihedral Mn_b−O−Mn_b−O angle, and (e) out-of-plane shift of the Mn_w atoms. Black (J_{bb}) and red (J_{wb}) open symbols are experimental J values of **9** (squares), **10** (triangles), **11** (stars), and **12** (pentagons) (Class 2).

In summary, the analysis of the dependence of the exchange interactions on the structural parameters signifies that the body−body interaction is strongly dependent on the Mn_b−O−Mn_b angle and the wing−body interactions is strongly dependent on Mn_b−O−Mn_b−O dihedral angle for both Class 1 and Class 2, causing variations in the J magnetic exchange parameters and therefore the observed magnetic properties. Although only minor variations are noted among the dihedral angles in the structures studied here, for other structure topology and in the polynuclear framework where this parameter is significantly different, this interaction may become relevant. To validate our developed correlations, we compared the reported (Class 1, see Table 3) J_{bb} values with the Mn_b−O−Mn_b angle and the J_{wb} values with the Mn_b−O−Mn_b−O angle (see Figure 9c and 9d). Our predictions are in good agreement with these previously reported J values.

CONCLUSIONS

We successfully synthesized and studied 12 mixed-valent $\{Mn^{II}_2Mn^{III}_2\}$ manganese complexes which display a butterfly metallic core. These compounds are classified by the position of the ions in the metallic core. Two distinct structural types are

DOI: 10.1021/acs.inorgchem.6b02527
Inorg. Chem. 2017, 56, 1932−1949

Table 5. Average Bond Distances (Angstroms) and Bond Angles (Degrees) That Can Affect the Exchange Interactions of the {Mn_4} Complexes (see Figure 9)

Complex	Mn_b–O	Mn_w–O	α	γ	β
1	2.11	2.27	99.4	0	102.8
2	2.12	2.35	100.1	0	100.7
3	2.09	2.32	99.3	0	99.1
4	2.10	2.27	96.4	0	100.8
5	2.09	2.31	97.5	0	98.2
6	2.09	2.39	99.9	0	99.7
7	2.11	2.26	101.1	0	100.1
8	2.10	2.46	100.1	0	98.6
9	2.35	1.94	100.9	0	106.6
10	2.33	1.95	95.6	2.1	112.6
11	2.33	1.92	102.0	0	108.1
12	2.43	1.93	99.9	0	107.4

observed and denoted as Class 1 and Class 2. Class 1 compounds place the Mn(III) ions in the body positions of the butterfly metallic core, while the Mn(II) ions occupy the outer wing sites. Class 2 complexes display the reverse arrangement of ions, with the Mn(II) sites in the body positions and the Mn(III) ions occupying the outer wing sites. Magnetic measurements revealed differing magnetic exchange coupling parameters for each complex, and compounds **1**–**9** and **11** display slow magnetization relaxation, suggesting that they are single-molecule magnets.

In-depth, magnetic analysis of the 12 complexes revealed the following. In general, the extracted experimentally fitted and the DFT-calculated J values yield the following conclusions. (i) DFT can be used as an excellent tool for determining the nature of magnetic exchange interactions within polynuclear manganese-based complexes. (ii) From both experiment and theory it is found the wing–body J_{wb} coupling parameter is moderately ferromagnetic in nature for all complexes (from −0.51 to 1.87 cm^{-1}), except for **7** and **8** (experimental fit) and **12** (DFT and fit) (see Table 1). (iii) The body–body interactions (J_{bb}) are generally ferromagnetic for Class 1 and antiferromagnetic for Class 2. This J_{bb} pathway (Mn^{III}–Mn^{III}) is also generally the strongest interaction for Class 1 complexes (from −0.06 to +2.32 cm^{-1}). (iv) The wing–wing (J_{ww}) coupling constant, determined via DFT only, is found to show weak antiferromagnetic values for all complexes, except in **10** and **12**, which are weakly ferromagnetic. (v) The spin ground state is generally found to be larger for Class 1 than Class 2. This due to the fact that some of the body–body {Mn^{II}–Mn^{II}} interactions for Class 2 complexes are weaker than the {Mn^{III}–Mn^{II}} wing–body interactions, leading to dominant antiferromagnetic coupling and a smaller ground state S value. (vi) DFT calculations yield negative D values for all complexes. This suggests that if the spin ground state is large, slow relaxation of the magnetization will be observed. The magnitude of D was also found to be significantly influenced by the electron-donating/withdrawing substituents of the ligands.

In line with the theoretical predictions, complexes **1**, **2**, **3**, **6**, and **9** display clear SMM behavior, displaying peak maxima in the χ_M'' vs T plots, allowing for determination of the anisotropy barrier (U_{eff}). The order of the size of the energy barrier is **3** ≈ **6** > **1** > **2** ≈ **9**. The DFT-computed energy barriers (taking into account the computed D and the ground state S value) are also in line with the experimental value for **2**, **3**, and **6** and slightly underestimated for **1** and **9** (see Table S5).

Our calculations indicate that by attaching electron-withdrawing and -donating substituent's on the bridging carboxylates or peripheral ligands one can alter the nature of the magnetic exchange interaction, J, and thus the ground state and importantly also the anisotropy. The Class 1 complexes possessing {$Mn^{III}(OR)_2$} interactions at the body positions are superior compared to their Mn^{II} counterparts as these body–body interactions are found to control the sign and strength of the J parameters as well as the magnetic anisotropy. The developed magneto-structural correlations suggest possible future ways to enhance the J's by fine tuning the Mn_b–O–Mn_b and Mn_b–O–Mn_b–O parameters in these {Mn_4} butterfly systems.

■ ASSOCIATED CONTENT

Supporting Information

The Supporting Information is available free of charge on the ACS Publications website at DOI: 10.1021/acs.inorgchem.6b02527.

Crystallographic data; bond valence sum values; bond lengths and angles; computed ZFS parameters; energy barrier values; computed ground and first excited spin state values; spin configurations employed for extracting J values; molecular structures of **2**–**8** and **10**–**12**; packing diagram of **1**–**12**; ac susceptibility plots; Arrhenius plots; susceptibility plots of **1**–**12**; orbital orientations (PDF)
Crystallographic data in CIF format (ZIP)

■ AUTHOR INFORMATION

Corresponding Authors

*E-mail: keith.murray@monash.edu.
*E-mail: rajaraman@chem.iitb.ac.in.

ORCID

Gopalan Rajaraman: 0000-0001-6133-3026

Notes

The authors declare no competing financial interest.

■ ACKNOWLEDGMENTS

G.R. would like to acknowledge the financial support from DST India and IIT Bombay for the high-performance computing facility. K.R.V. and G.R. acknowledge the C-DAC's Supercomputing resources (PARAM Yuva-II). K.R.V. is thankful to the IITB-Monash Research Academy for a Ph.D. studentship. G.R. and K.S.M. acknowledge the support of an Australia-India Strategic Research Fund (AISRF) grant.

■ REFERENCES

(1) (a) Murray, K. S. In *The Magnetochemistry of Homo-and Hetero-Tetranuclear First-Row d-Block Complexes*; Sykes, A. G., Ed.; Academic Press: 1995; Vol. Vol. *43*, pp 261–358. (b) Albela, B.; El Fallah, M. S.; Ribas, J.; Folting, K.; Christou, G.; Hendrickson, D. N. Two New Mixed-Valence Manganese Complexes of Formula [Mn_4O_2(X-benzoato)$_7$(bpy)$_2$] (X = 2-Cl, 2-Br) and the Crystal Structure of the 2-Cl Complex: Ground-State Spin Variability in the $[Mn_4O_2]^{7+}$ Complexes. *Inorg. Chem.* **2001**, *40*, 1037–1044. (c) Yang, C.-I.; Lee, G.-H.; Wur, C.-S.; Lin, J. G.; Tsai, H.-L. Syntheses, structures and single-molecule magnetic behaviors of two dicubane Mn_4 complexes. *Polyhedron* **2005**, *24*, 2215–2221. (d) Yoo, J.; Yamaguchi, A.; Nakano, M.; Krzystek, J.; Streib, W. E.; Brunel, L.-C.; Ishimoto, H.; Christou, G.; Hendrickson, D. N. Mixed-Valence Tetranuclear Manganese Single-Molecule Magnets. *Inorg. Chem.* **2001**, *40*, 4604–4616. (e) Lecren, L.; Li, Y.-G.; Wernsdorfer, W.; Roubeau, O.; Miyasaka, H.; Clérac, R. $[Mn_4(hmp)_6(CH_3CN)_2(H_2O)_4]^{4+}$: A new single-

DOI: 10.1021/acs.inorgchem.6b02527
Inorg. Chem. 2017, 56, 1932–1949

molecule magnet with the highest blocking temperature in the Mn4/hmp family of compounds. *Inorg. Chem. Commun.* **2005**, *8*, 626−630. (f) Lecren, L.; Roubeau, O.; Li, Y.-G.; Le Goff, X. F.; Miyasaka, H.; Richard, F.; Wernsdorfer, W.; Coulon, C.; Clerac, R. One-dimensional coordination polymers of antiferromagnetically-coupled [Mn_4] single-molecule magnets. *Dalton Trans.* **2008**, 755−766. (g) Yang, E.-C.; Harden, N.; Wernsdorfer, W.; Zakharov, L.; Brechin, E. K.; Rheingold, A. L.; Christou, G.; Hendrickson, D. N. Mn4 single-molecule magnets with a planar diamond core and S = 9. *Polyhedron* **2003**, *22*, 1857−1863. (h) Langley, S. K.; Chilton, N. F.; Massi, M.; Moubaraki, B.; Berry, K. J.; Murray, K. S. Synthesis and characterization of homo- and heterovalent tetra- hexa- hepta- and decanuclear manganese clusters using pyridyl functionalized [small beta]-diketone, carboxylate and triethanolamine ligands. *Dalton Trans.* **2010**, *39*, 7236−7249. (i) Langley, S. K.; Chilton, N. F.; Moubaraki, B.; Murray, K. S. Structure and magnetic exchange in heterometallic 3d-3d transition metal triethanolamine clusters. *Dalton Trans.* **2012**, *41*, 1033−1046. (j) Wittick, L. M.; Jones, L. F.; Jensen, P.; Moubaraki, B.; Spiccia, L.; Berry, K. J.; Murray, K. S. New mixed-valence $Mn^{II}_2Mn^{III}_2$ clusters exhibiting an unprecedented $Mn^{II/III}$ oxidation state distribution in their magnetically coupled cores. *Dalton Trans.* **2006**, 1534−1543. (k) Lecren, L.; Roubeau, O.; Coulon, C.; Li, Y.-G.; Le Goff, X. F.; Wernsdorfer, W.; Miyasaka, H.; Clérac, R. Slow Relaxation in a One-Dimensional Rational Assembly of Antiferromagnetically Coupled [Mn_4] Single-Molecule Magnets. *J. Am. Chem. Soc.* **2005**, *127*, 17353−17363. (l) Yoo, J.; Brechin, E. K.; Yamaguchi, A.; Nakano, M.; Huffman, J. C.; Maniero, A. L.; Brunel, L.-C.; Awaga, K.; Ishimoto, H.; Christou, G.; Hendrickson, D. N. Single-Molecule Magnets: A New Class of Tetranuclear Manganese Magnets. *Inorg. Chem.* **2000**, *39*, 3615−3623. (m) Miyasaka, H.; Nakata, K.; Lecren, L.; Coulon, C.; Nakazawa, Y.; Fujisaki, T.; Sugiura, K.-i.; Yamashita, M.; Clérac, R. Two-Dimensional Networks Based on Mn4 Complex Linked by Dicyanamide Anion: From Single-Molecule Magnet to Classical Magnet Behavior. *J. Am. Chem. Soc.* **2006**, *128*, 3770−3783. (n) Brechin, E. K.; Huffman, J. C.; Christou, G.; Yoo, J.; Nakano, M.; Hendrickson, D. N. A new class of single-molecule magnets: mixed-valent [$Mn_4(O_2CMe)_2(Hpdm)_6$][ClO_4]$_2$ with an S = 8 ground state. *Chem. Commun.* **1999**, 783−784. (o) Wittick, L. M.; Murray, K. S.; Moubaraki, B.; Batten, S. R.; Spiccia, L.; Berry, K. J. Synthesis, structure and magnetism of new single molecule magnets composed of $Mn^{II}_2Mn^{III}_2$ alkoxo-carboxylate bridged clusters capped by triethanolamine ligands. *Dalton Trans.* **2004**, 1003−1011. (p) Yoo, J.; Wernsdorfer, W.; Yang, E.-C.; Nakano, M.; Rheingold, A. L.; Hendrickson, D. N. One-Dimensional Chain of Tetranuclear Manganese Single-Molecule Magnets. *Inorg. Chem.* **2005**, *44*, 3377−3379. (q) Hiraga, H.; Miyasaka, H.; Nakata, K.; Kajiwara, T.; Takaishi, S.; Oshima, Y.; Nojiri, H.; Yamashita, M. Hybrid Molecular Material Exhibiting Single-Molecule Magnet Behavior and Molecular Conductivity. *Inorg. Chem.* **2007**, *46*, 9661−9671. (r) Miyasaka, H.; Nakata, K.; Sugiura, K.-i.; Yamashita, M.; Clérac, R. A Three-Dimensional Ferrimagnet Composed of Mixed-Valence Mn_4 Clusters Linked by an $\{Mn[N(CN)_2]_6\}^{4-}$ Unit. *Angew. Chem., Int. Ed.* **2004**, *43*, 707−711. (s) Lecren, L.; Wernsdorfer, W.; Li, Y.-G.; Roubeau, O.; Miyasaka, H.; Clérac, R. Quantum Tunneling and Quantum Phase Interference in a [$Mn^{II}_2Mn^{III}_2$] Single-Molecule Magnet. *J. Am. Chem. Soc.* **2005**, *127*, 11311−11317. (t) Lu, Z.; Fan, C. A novel tetranuclear $Mn^{II}_2Mn^{III}_2$ cluster [$Mn_4(hmp)_6(N_3)_4$]: Synthesis, crystal structure and magnetic properties. *Inorg. Chem. Commun.* **2011**, *14*, 1329−1332. (u) Ako, A. M.; Mereacre, V.; Hewitt, I. J.; Clerac, R.; Lecren, L.; Anson, C. E.; Powell, A. K. Enhancing single molecule magnet parameters. Synthesis, crystal structures and magnetic properties of mixed-valent Mn_4 SMMs. *J. Mater. Chem.* **2006**, *16*, 2579−2586. (v) Karotsis, G.; Teat, S. J.; Wernsdorfer, W.; Piligkos, S.; Dalgarno, S. J.; Brechin, E. K. Calix[4]arene-based single-molecule magnets. *Angew. Chem., Int. Ed.* **2009**, *48*, 8285−8288. (w) Taylor, S. M.; Karotsis, G.; McIntosh, R. D.; Kennedy, S.; Teat, S. J.; Beavers, C. M.; Wernsdorfer, W.; Piligkos, S.; Dalgarno, S. J.; Brechin, E. K. A Family of Calix[4]arene supported [$Mn^{III}_2Mn^{II}_2$] Clusters. *Chem. - Eur. J.* **2011**, *17*, 7521−7530. (x) Palacios, M. A.; McLellan, R.; Beavers, C. M.; Teat, S. J.; Weihe, H.; Piligkos, S.; Dalgarno, S. J.; Brechin, E. K. Facile interchange of 3*d* and 4*f* ions in Single-Molecule Magnets: stepwise assembly of [Mn_4], [Mn_3Ln] and [Mn_2Ln_2] cages within calix[4]arene scaffolds. *Chem. - Eur. J.* **2015**, *21*, 11212−11218.

(2) (a) Wang, M.; Ma, C.-B.; Yuan, D.-Q.; Wang, H.-S.; Chen, C.-N.; Liu, Q.-T. Synthesis and Characterization of a Family of Penta- and Tetra-Manganese(III) Complexes Derived from an Assembly System Containing tert-Butylphosphonic Acid. *Inorg. Chem.* **2008**, *47*, 5580−5590. (b) Wemple, M. W.; Tsai, H.-L.; Wang, S.; Claude, J. P.; Streib, W. E.; Huffman, J. C.; Hendrickson, D. N.; Christou, G. Tetranuclear and Octanuclear Manganese Carboxylate Clusters: Preparation and Reactivity of ($NBun_4$)[$Mn_4O_2(O_2CPh)_9(H_2O)$] and Synthesis of ($NBun_4$)$_2$[$Mn_8O_4(O_2CPh)_{12}(Et_2mal)_2(H_2O)_2$] with a "Linked-Butterfly" Structure. *Inorg. Chem.* **1996**, *35*, 6437−6449. (c) Ruettinger, W.; Yagi, M.; Wolf, K.; Bernasek, S.; Dismukes, G. C. O_2 Evolution from the Manganese−Oxo Cubane Core $Mn_4O_4^{6+}$: A Molecular Mimic of the Photosynthetic Water Oxidation Enzyme? *J. Am. Chem. Soc.* **2000**, *122*, 10353−10357. (d) Hendrickson, D. N.; Christou, G.; Schmitt, E. A.; Libby, E.; Bashkin, J. S.; Wang, S.; Tsai, H. L.; Vincent, J. B.; Boyd, P. D. W. Photosynthetic water oxidation center: spin frustration in distorted cubane $Mn^{IV}Mn^{III}_3$ model complexes. *J. Am. Chem. Soc.* **1992**, *114*, 2455−2471.

(3) (a) Gatteschi, D.; Sessoli, R. Quantum Tunneling of Magnetization and Related Phenomena in Molecular Materials. *Angew. Chem., Int. Ed.* **2003**, *42*, 268−297. (b) Sessoli, R.; Gatteschi, D.; Caneschi, A.; Novak, M. A. Magnetic Bistability in a Metal-Ion Cluster. *Nature* **1993**, *365*, 141−143. (c) Sessoli, R.; Tsai, H. L.; Schake, A. R.; Wang, S.; Vincent, J. B.; Folting, K.; Gatteschi, D.; Christou, G.; Hendrickson, D. N. High-spin molecules: [$Mn_{12}O_{12}(O_2CR)_{16}(H_2O)_4$]. *J. Am. Chem. Soc.* **1993**, *115*, 1804−1816.

(4) (a) Gatteschi, D.; Sessoli, R.; Villain, J. *Molecular Nanomagnets*; Oxford University Press: Oxford, 2006. (b) Molecular spintronics and quantum computing. *J. Mater. Chem.* **2009**, *19*, 1670−1671. (c) Leuenberger, M. N.; Loss, D. Quantum computing in molecular magnets. *Nature* **2001**, *410*, 789−793. (d) Bogani, L.; Wernsdorfer, W. Molecular spintronics using single-molecule magnets. *Nat. Mater.* **2008**, *7*, 179−186. (e) Evangelisti, M.; Brechin, E. K. Recipes for enhanced molecular cooling. *Dalton Trans.* **2010**, *39*, 4672−4676. (f) Karotsis, G.; Kennedy, S.; Teat, S. J.; Beavers, C. M.; Fowler, D. A.; Morales, J. J.; Evangelisti, M.; Dalgarno, S. J.; Brechin, E. K. [$Mn^{III}_4Ln^{III}_4$] Calix[4]arene Clusters as Enhanced Magnetic Coolers and Molecular Magnets. *J. Am. Chem. Soc.* **2010**, *132*, 12983−12990.

(5) Roubeau, O.; Clérac, R. Rational Assembly of High-Spin Polynuclear Magnetic Complexes into Coordination Networks: the Case of a [Mn_4] Single-Molecule Magnet Building Block. *Eur. J. Inorg. Chem.* **2008**, *2008*, 4325−4342.

(6) (a) McCusker, J. K.; Vincent, J. B.; Schmitt, E. A.; Mino, M. L.; Shin, K.; Coggin, D. K.; Hagen, P. M.; Huffman, J. C.; Christou, G.; Hendrickson, D. N. Molecular spin frustration in the $[Fe_4O_2]^{8+}$ core: synthesis, structure, and magnetochemistry of tetranuclear iron-oxo complex [$Fe_4O_2(O_2CR)_7(bpy)_2$]($C1O_4$) (R = Me, Ph). *J. Am. Chem. Soc.* **1991**, *113*, 3012−3021. (b) Hriljac, J. A.; Harris, S.; Shriver, D. F. Protonation and bonding in heterometallic butterfly carbide clusters. *Inorg. Chem.* **1988**, *27*, 816−821. (c) Boudalis, A. K.; Lalioti, N.; Spyroulias, G. A.; Raptopoulou, C. P.; Terzis, A.; Bousseksou, A.; Tangoulis, V.; Tuchagues, J.-P.; Perlepes, S. P. Novel Rectangular $[Fe_4(\mu_4\text{-}OHO)(\mu\text{-}OH)_2]^{7+}$ versus "Butterfly" $[Fe_4(\mu_3\text{-}O)_2]^{8+}$ Core Topology in the FeIII/RCO2-/phen Reaction Systems (R = Me, Ph; phen = 1,10-Phenanthroline): Preparation and Properties of [$Fe_4(OHO)(OH)_2(O_2CMe)_4(phen)_4$]($ClO_4$)$_3$, [$Fe_4O_2(O_2CPh)_7(phen)_2$]($ClO_4$), and [$Fe_4O_2(O_2CPh)_8(phen)_2$]. *Inorg. Chem.* **2002**, *41*, 6474−6487. (d) Castro, S. L.; Sun, Z.; Grant, C. M.; Bollinger, J. C.; Hendrickson, D. N.; Christou, G. Single-Molecule Magnets: Tetranuclear Vanadium(III) Complexes with a Butterfly Structure and an S = 3 Ground State. *J. Am. Chem. Soc.* **1998**, *120*, 2365−2375. (e) Liu, Q.; Yang, Y.; Huang, L.; Wu, D.; Kang, B.; Chen, C.; Deng, Y.; Lu, J. Study on an Assembly System Including Tetrathiovanadate. Syntheses and Structural Characterizations of V2Cu2S4 Cubane-Like Clusters and VS4Cu4 Bimetallic Aggregates.

DOI: 10.1021/acs.inorgchem.6b02527
Inorg. Chem. 2017, 56, 1932−1949

Inorg. Chem. **1995**, *34*, 1884−1893. (f) Sunatsuki, Y.; Shimada, H.; Matsuo, T.; Nakamura, M.; Kai, F.; Matsumoto, N.; Re, N. Synthesis, Magnetic Properties, and Incomplete Double-Cubane Structure of Manganese(III)−Metal(II) Complexes [Mn(MeOH)L(OH)M(bpy)]$_2$ (M = Zn, Cu, Ni, and Mn; H_4L = 1,2-Bis(2-hydroxybenzamido)benzene; bpy = 2,2′-Bipyridine. *Inorg. Chem.* **1998**, *37*, 5566−5574. (g) Papatriantafyllopoulou, C.; Abboud, K. A.; Christou, G. Carboxylate-Free $Mn^{III}_2Ln^{III}_2$ (Ln = Lanthanide) and $Mn^{III}_2Y^{III}_2$ Complexes from the Use of (2-Hydroxymethyl)pyridine: Analysis of Spin Frustration Effects. *Inorg. Chem.* **2011**, *50*, 8959−8966.

(7) Vincent, J. B.; Chang, H. R.; Folting, K.; Huffman, J. C.; Christou, G.; Hendrickson, D. N. Preparation and physical properties of trinuclear oxo-centered manganese complexes of general formulation $[Mn_3O(O_2CR)_6L_3]^{0,+}$ (R = methyl or phenyl; L = a neutral donor group) and the crystal structures of $[Mn_3O(O_2CMe)_6(pyr)_3](pyr)$ and $[Mn_3O(O_2CPh)_6(pyr)_2(H_2O)]$. cntdot.0.5MeCN. *J. Am. Chem. Soc.* **1987**, *109*, 5703−5711.

(8) Sheldrick, G. A short history of SHELX. *Acta Crystallogr., Sect. A: Found. Crystallogr.* **2008**, *64*, 112−122.

(9) Sheldrick, G. M. *SHELXL-97, Programs for X-ray Crystal Structure Refinement*; University of Göttingen: Göttingen, Germany, 1997.

(10) Barbour, L. J. *J. Supramol. Chem.* **2001**, *1*, 189−191.

(11) (a) Bencini, A.; Totti, F. DFT description of the magnetic structure of polynuclear transition-metal clusters: The complexes $[\{Cu(bpca)_2(H_2O)_2\}\{Cu(NO_3)_2\}_2]$, (bpca = Bis(2-pyridylcarbonyl)-amine), and $[Cu(DBSQ)(C_2H_5O)]_2$, (DBSQ = 3,5-di-tert-butyl-semiquinonato). *Int. J. Quantum Chem.* **2005**, *101*, 819−825. (b) Comba, P.; Hausberg, S.; Martin, B. Calculation of exchange coupling constants of transition metal complexes with DFT. *J. Phys. Chem. A* **2009**, *113*, 6751−6755.

(12) Noodleman, L. Valence bond description of antiferromagnetic coupling in transition metal dimers. *J. Chem. Phys.* **1981**, *74*, 5737−5743.

(13) (a) Christian, P.; Rajaraman, G.; Harrison, A.; Helliwell, M.; McDouall, J. J. W.; Raftery, J.; Winpenny, R. E. P. Synthesis and studies of a trinuclear Mn(ii) carboxylate complex. *Dalton Trans.* **2004**, 2550−2555. (b) Rajaraman, G.; Cano, J.; Brechin, E. K.; McInnes, E. J. L. Density functional calculations of a tetradecametallic iron(iii) cluster with a very large spin ground state. *Chem. Commun.* **2004**, 1476−1477. (c) Ruiz, E.; Rodríguez-Fortea, A.; Cano, J.; Alvarez, S.; Alemany, P. About the calculation of exchange coupling constants in polynuclear transition metal complexes. *J. Comput. Chem.* **2003**, *24*, 982−989. (d) Baker, M. L.; Timco, G. A.; Piligkos, S.; Mathieson, J. S.; Mutka, H.; Tuna, F.; Kozlowski, P.; Antkowiak, M.; Guidi, T.; Gupta, T.; Rath, H.; Woolfson, R. J.; Kamieniarz, G.; Pritchard, R. G.; Weihe, H.; Cronin, L.; Rajaraman, G.; Collison, D.; McInnes, E. J. L.; Winpenny, R. E. P. A classification of spin frustration in molecular magnets from a physical study of large odd-numbered-metal, odd electron rings. *Proc. Natl. Acad. Sci. U. S. A.* **2012**, *109*, 19113−19118. (e) Christian, P.; Rajaraman, G.; Harrison, A.; McDouall, J. J. W.; Raftery, J. T.; Winpenny, R. E. P. Structural, magnetic and DFT studies of a hydroxide-bridged $\{Cr_8\}$ wheel. *Dalton Trans.* **2004**, 1511−1512. (f) Cremades, E.; Cano, J.; Ruiz, E.; Rajaraman, G.; Milios, C. J.; Brechin, E. K. Theoretical Methods Enlighten Magnetic Properties of a Family of Mn_6 Single-Molecule Magnets. *Inorg. Chem.* **2009**, *48*, 8012−8019. (g) Vignesh, K. R.; Langley, S. K.; Moubaraki, B.; Murray, K. S.; Rajaraman, G. Large Hexadecametallic $\{Mn^{III}−Ln^{III}\}$ Wheels: Synthesis, Structural, Magnetic, and Theoretical Characterization. *Chem. - Eur. J.* **2015**, *21*, 16364−16369. (h) Vignesh, K. R.; Langley, S. K.; Murray, K. S.; Rajaraman, G. What Controls the Magnetic Exchange Interaction in Mixed- and Homo-Valent Mn_7 Disc-Like Clusters? A Theoretical Perspective. *Chem. - Eur. J.* **2015**, *21*, 2881−2892.

(14) Becke, A. D. Density functional thermochemistry. III. The role of exact exchange. *J. Chem. Phys.* **1993**, *98*, 5648−5652.

(15) (a) Schaefer, A.; Horn, H.; Ahlrichs, R. Fully optimized contracted Gaussian basis sets for atoms Li to Kr. *J. Chem. Phys.* **1992**, *97*, 2571−2577. (b) Schaefer, A.; Huber, C.; Ahlrichs, R. Fully optimized contracted Gaussian basis sets of triple zeta valence quality for atoms Li to Kr. *J. Chem. Phys.* **1994**, *100*, 5829−5835.

(16) Frisch, M. J.; Trucks, G. W.; Schlegel, H. B.; Scuseria, G. E.; Robb, M. A.; Cheeseman, J. R.; Scalmani, G.; Barone, V.; Mennucci, B.; Petersson, G. A.; Nakatsuji, H.; Caricato, M.; Li, X.; Hratchian, H. P.; Izmaylov, A. F.; Bloino, J.; Zheng, G.; Sonnenberg, J. L.; Hada, M.; Ehara, M.; Toyota, K.; Fukuda, R.; Hasegawa, J.; Ishida, M.; Nakajima, T.; Honda, Y.; Kitao, O.; Nakai, H.; Vreven, T.; Montgomery, J. A., Jr.; Peralta, J. E.; Ogliaro, F.; Bearpark, M.; Heyd, J. J.; Brothers, E.; Kudin, K. N.; Staroverov, V. N.; Kobayashi, R.; Normand, J.; Raghavachari, K.; Rendell, A.; Burant, J. C.; Iyengar, S. S.; Tomasi, J.; Cossi, M.; Rega, N.; Millam, J. M.; Klene, M.; Knox, J. E.; Cross, J. B.; Bakken, V.; Adamo, C.; Jaramillo, J.; Gomperts, R.; Stratmann, R. E.; Yazyev, O.; Austin, A. J.; Cammi, R.; Pomelli, C.; Ochterski, J. W.; Martin, R. L.; Morokuma, K.; Zakrzewski, V. G.; Voth, G. A.; Salvador, P.; Dannenberg, J. J.; Dapprich, S.; Daniels, A. D.; Farkas, Ö; Foresman, J. B.; Ortiz, J. V.; Cioslowski, J.; Fox, D. J. *Gaussian 09*, R. A.02; Gaussian, Inc., Wallingford, CT, 2009.

(17) Chilton, N. F.; Anderson, R. P.; Turner, L. D.; Soncini, A.; Murray, K. S. PHI: A powerful new program for the analysis of anisotropic monomeric and exchange-coupled polynuclear d- and f-block complexes. *J. Comput. Chem.* **2013**, *34*, 1164−1175.

(18) Neese, F. The ORCA program system. *WIREs Comput. Mol. Sci.* **2012**, *2*, 73−78.

(19) (a) Berg, N.; Hooper, T. N.; Liu, J.; Beedle, C. C.; Singh, S. K.; Rajaraman, G.; Piligkos, S.; Hill, S.; Brechin, E. K.; Jones, L. F. Synthetic, structural, spectroscopic and theoretical study of a Mn(iii)-Cu(ii) dimer containing a Jahn-Teller compressed Mn ion. *Dalton Trans.* **2013**, *42*, 207−216. (b) Singh, S. K.; Gupta, T.; Badkur, P.; Rajaraman, G. Magnetic Anisotropy of Mononuclear NiII Complexes: On the Importance of Structural Diversity and the Structural Distortions. *Chem. - Eur. J.* **2014**, *20*, 10305−10313. (c) Singh, S. K.; Rajaraman, G. Probing the Origin of Magnetic Anisotropy in a Dinuclear $\{Mn^{III}Cu^{II}\}$ Single-Molecule Magnet: The Role of Exchange Anisotropy. *Chem. - Eur. J.* **2014**, *20*, 5214−5218. (d) Singh, S. K.; Rajaraman, G. Can anisotropic exchange be reliably calculated using density functional methods? a case study on trinuclear Mn^{III}-M^{III}-Mn^{III} (M = Fe, Ru, and Os) cyanometalate single-molecule magnets. *Chem. - Eur. J.* **2014**, *20*, 113−123. (e) Sinnecker, S.; Neese, F.; Noodleman, L.; Lubitz, W. Calculating the Electron Paramagnetic Resonance Parameters of Exchange Coupled Transition Metal Complexes Using Broken Symmetry Density Functional Theory: Application to a Mn^{III}/Mn^{IV} Model Compound. *J. Am. Chem. Soc.* **2004**, *126*, 2613−2622.

(20) (a) Langley, S. K.; Chilton, N. F.; Ungur, L.; Moubaraki, B.; Chibotaru, L. F.; Murray, K. S. Heterometallic Tetranuclear $[Ln^{III}_2Co^{III}_2]$ Complexes Including Suppression of Quantum Tunneling of Magnetization in the $[Dy^{III}_2Co^{III}_2]$ Single Molecule Magnet. *Inorg. Chem.* **2012**, *51*, 11873−11881. (b) Langley, S. K.; Moubaraki, B.; Murray, K. S. A heptadecanuclear $Mn^{III}_9Dy^{III}_8$ cluster derived from triethanolamine with two edge sharing supertetrahedra as the core and displaying SMM behaviour. *Dalton Trans.* **2010**, *39*, 5066−5069. (c) Langley, S. K.; Ungur, L.; Chilton, N. F.; Moubaraki, B.; Chibotaru, L. F.; Murray, K. S. Single-Molecule Magnetism in a Family of $\{Co^{III}_2Dy^{III}_2\}$ Butterfly Complexes: Effects of Ligand Replacement on the Dynamics of Magnetic Relaxation. *Inorg. Chem.* **2014**, *53*, 4303−4315.

(21) Liu, W.; Thorp, H. H. Bond valence sum analysis of metal-ligand bond lengths in metalloenzymes and model complexes. 2. Refined distances and other enzymes. *Inorg. Chem.* **1993**, *32*, 4102−4105.

(22) Berg, N.; Rajeshkumar, T.; Taylor, S. M.; Brechin, E. K.; Rajaraman, G.; Jones, L. F. What Controls the Magnetic Interaction in bis-μ-Alkoxo Mn^{III} Dimers? A Combined Experimental and Theoretical Exploration. *Chem. - Eur. J.* **2012**, *18*, 5906−5918.

(23) (a) Singh, S. K.; Gupta, T.; Rajaraman, G. Magnetic Anisotropy and Mechanism of Magnetic Relaxation in Er(III) Single-Ion Magnets. *Inorg. Chem.* **2014**, *53*, 10835−10845. (b) Singh, S. K.; Gupta, T.; Shanmugam, M.; Rajaraman, G. Unprecedented magnetic relaxation via the fourth excited state in low-coordinate lanthanide single-ion

DOI: 10.1021/acs.inorgchem.6b02527
Inorg. Chem. 2017, 56, 1932−1949

magnets: a theoretical perspective. *Chem. Commun.* **2014**, *50*, 15513−15516. (c) Singh, S. K.; Gupta, T.; Ungur, L.; Rajaraman, G. Magnetic Relaxation in Single-Electron Single-Ion Cerium(III) Magnets: Insights from Ab Initio Calculations. *Chem. - Eur. J.* **2015**, *21*, 13812−13819.

(24) Cauchy, T.; Ruiz, E.; Alvarez, S. Magnetostructural Correlations in Polynuclear Complexes: The Fe_4 Butterflies. *J. Am. Chem. Soc.* **2006**, *128*, 15722−15727.

DOI: 10.1021/acs.inorgchem.6b02527
Inorg. Chem. 2017, 56, 1932−1949